Super-oscillatory lenses and optical metasurfaces

MASTER RESEARCH PROJECT

November 17, 2015

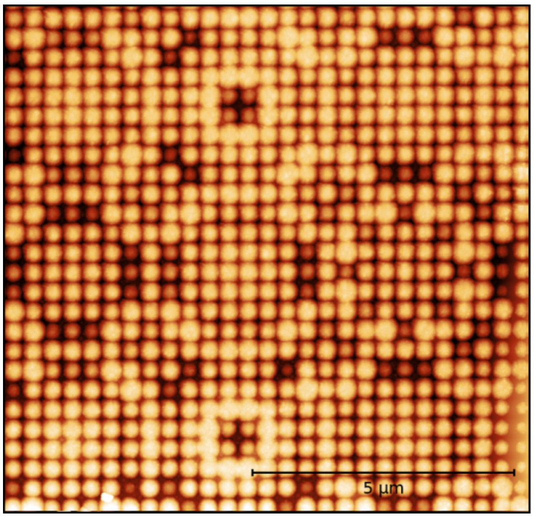

Author:
Kim Vendel
Student ID:
0778958

Supervisors:
Prof. Dr. Ir. Giampiero Gerini
Dr. Ir. Stefan Bäumer
Fabrizio Silvestri MSc
Prof. Dr. Martin van Exter

Contents

Introduction

Since ancient times, people have manufactured and used optical devices like lenses, mirrors and polarizers. A conventional lens is a refracting device that reshapes the wavefront of light while it is transmitted through the medium [1]. More recently, "new" optical devices have been proposed to go beyond conventional optics. One famous example is the Pendry-Veselago negative refractive index superlens [2]. In this project, we study two types of unconventional optical devices: a super-oscillatory lens (SOL) and optical metasurfaces (OM).

A SOL is a nanostructured mask consisting of subwavelength binary amplitude concentric rings, which creates an interference pattern with a central hotspot and several sidebands. The size of this hotspot can be (much) smaller than the focal spot of a diffraction limited conventional lens. The SOL is part of a larger project within TNO: Beyond Conventional Optics and the META-instrument. The final goal is to perform non-invasive super-resolution imaging. This is useful for fast and accurate inspection of nanostructures or contamination on wafers.

Optical metasurfaces are based on a completely different concept. A metasurface is an artificial periodic structure that exhibits different behavior from natural materials. Our sample consists of an array of cylindrical silicon (Si) resonators embedded in fused silica (SiO_2). Since these resonators have subwavelength dimensions, their scattered field can in first order be described by electric and magnetic dipoles. By tailoring the individual resonators in the array, a specific phase profile can be imposed on the incident light. The goal is to design and produce optical devices that can have similar performance as conventional optics (high NA, diffraction limited, good signal to noise ratio), but that are extremely thin. An application for such compact optical devices are integrated sensors and on-chip devices.

In this thesis, we will describe the characterization of a SOL and several optical metasurfaces, like lenses, quarter waveplates and polarization scramblers. In chapter 1 we present an overview of the theory and of the state of the art. Next, in chapter 2 the samples, setup, measuring procedures and data analysis for both types of non-conventional optics are explained. The results of experiments with the SOL are shown and discussed in chapter 3 and the same is done for the optical metasurfaces in chapter 4. Finally, some general conclusions are drawn in chapter 5.

Chapter 1

Theory

A conventional lens is a refracting device that reshapes the wavefront of propagating light [1]. It relies on gradual phase accumulation along the optical path to change the wavefront, since the propagation velocity depends on the refractive index n of the lens. Therefore, a thin lens simply delays an incident wavefront by an amount proportional to the thickness of the lens at each point.

This type of lenses has been used for centuries, but there are some drawbacks. Examples are the lens dimensions and the diffraction limit. With the development of technology, the scale of components is getting smaller. At the moment, nanotechnology and on-chip devices are growing fields. To fit optical devices into such small platforms, it is necessary that they have limited dimensions as well. It is difficult and costly to manufacture conventional lenses with the desired dimensions and sufficient performance. In addition, to image smaller features, it would be of great benefit to have a lens that can image below the diffraction limit, since this is limiting conventional lenses.

Optical devices based on metamaterials (MM) or metasurfaces (MS) provide new opportunities to create optical devices that fulfill these requirements. Metamaterials are materials that do not occur in nature, but are designed and manufactured to have different properties compared to natural materials. Metasurfaces are 2D metamaterials, and therefore they are easier to design and manufacture.

One of the properties we would like to tailor is the spotsize of the focus of a lens, to go beyond the diffraction limit. The diffraction limit sets a lower limit to the resolution of a lens. Imaging a point source with a perfect conventional lens results in an Airy disc pattern: a central spot surrounded by circular sidebands. This is the result of diffraction of the light by the aperture of the lens. The spread of the light from a point source is called the point spread function (PSF) of an optical system. The Airy disk radius d is defined as the distance from the center of the spot to the first minimum, and gives a measure of the distance that two objects can be apart such that they can still be distinguished. This distance is given by the Rayleigh criterion [3]:

$$d = 1.22\frac{\lambda}{2\mathrm{NA}} \tag{1.1}$$

with λ the wavelength of the light and NA the numerical aperture of the lens ($\mathrm{NA} = n\,sin(\theta)$, where θ is the maximum acceptance angle of the lens).

The FWHM of the central spot of an Airy pattern gives a measure of the smallest spot that can be formed by a lens, and is given by

$$FWHM \approx \frac{\lambda}{2\mathrm{NA}}. \tag{1.2}$$

The spatial information of an object to be imaged is carried by propagating waves for the small frequencies (coarse features) and evanescent waves for high frequencies (fine details). Evanescent waves decay over the lengthscale of a wavelength, and can not be collected by a conventional lens.

A theory based on metamaterials has been developed to use evanescent waves to obtain super-resolution imaging: the Pendry-Veselago superlens [2]. This superlens is based on a metamaterial with a negative refractive index n, so the light is refracted with a negative angle compared to normal refraction as pictured in Fig. 1.1 and Fig. 1.2. A piece of negative index material behaves as negative space [4], and it has been observed that it focuses both the propagating and the evanescent components of the light [2]. In theory, this type of superlens can create a perfect image of an object. However, in order to collect the evanescent waves, the superlens needs to be positioned in the near field of the object. This increases the risk of touching and damaging the object or the lens. In addition, manufacturing of materials with a negative refractive index is still problematic, especially for wavelengths in the visible regime. Finally, for the negative index metamaterials that have been realized so far, optical losses were a significant problem since they are composed of multiple metal layers. Because of these downsides of negative index superlenses, different types of super-resolution lenses have been studied.

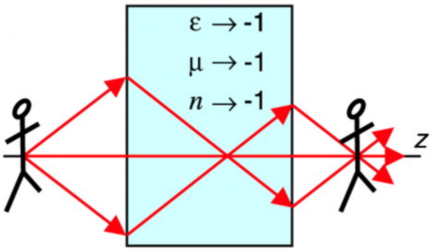

Figure 1.1: Schematic picture of the principle of the Pendry-Veselago superlens [4]. With a negative refractive index n, the light is refracted anomalously.

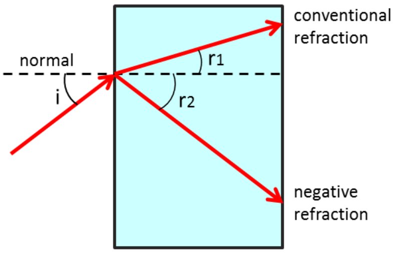

Figure 1.2: Example of the angle of refraction for a conventional material (r_1) and a negative refractive index material (r_2).

Berry and Popescu predicted in 2006 that diffraction off a grating structure could create spots with sizes below the diffraction limit at positions beyond the near-field of the structure. This could be interpreted as the propagation of information of sub-wavelength structures farther than evanescent waves [5]. The formation of those spots originates from so-called super-oscillations, as will be explained in Sec. 1.1.

Although it is useful and interesting to image below the diffraction limit, this is not the only purpose of non-conventional optical devices. Another promising property of these devices is that they are extremely thin, and can be designed to manipulate light in any desired way. For example, with arrays of subwavelength resonators, not only very thin lenses can be designed, but also polarizers, waveplates and polarization scramblers. More about metasurfaces for this purpose is described in Sec. 1.2.

1.1 Super-oscillatory lenses

A super-oscillatory lens (SOL) is a nanostructured mask, which creates an interference pattern consisting of a hotspot with multiple sidebands when it is illuminated with coherent light [6][7]. For a conventional lens, the full width half maximum (FWHM) of the spot is limited to approximately $\lambda/2$ (see Eq. 1.2 [3]) by the diffraction limit. The hotspot of a SOL can be smaller, since it is formed by so called super-oscillations [6]. It has been shown that bandlimited functions can locally vary faster than their fastest Fourier component [5][8]. This is called a super-oscillation. For example, a bandlimited function like

$$f(x) = \sum_n a_n cos(2\pi n x) \tag{1.3}$$

with $a_n = 0$ for $n > 5$ and specific values of a_n for $n \leq 5$ shows superoscillations around $x = 0$, as shown in Fig. 1.3. Typical properties of a super-oscillatory function are a low intensity and a rapidly oscillating phase in the super-oscillatory region [5].
Plane waves are generated by the transparent parts of the SOL mask, and those waves create an interference pattern in the far field. This field can be described by [9]

$$E(x, y, z) = \int F(u, v) e^{-i(ux+vy)} e^{iz\sqrt{k^2-u^2-v^2}} dudv \tag{1.4}$$

with k the wavevector of the light in a medium ($k = k_0 n$) and $F(u, v)$ the Fourier transform of the electromagnetic field at the plane of the SOL. Equation 1.4 is the continuous version of the super-oscillatory function from Eq. 1.3. This means that the frequencies in the interference pattern can be higher than those of the individual waves, and therefore a hotspot can be formed that is smaller than the $\lambda/2$NA from Eq. 1.2 [9]. The position where the FWHM of the hotspot is minimal is usually called the focus of the SOL.

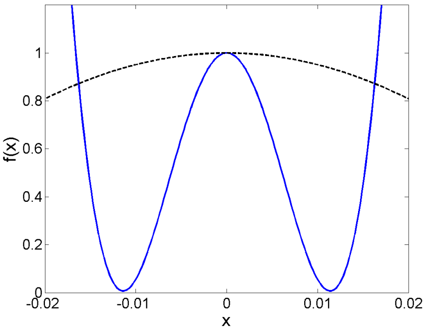

Figure 1.3: Example of a super-oscillatory function (adapted from [6]), where the bandlimited function (blue) from Eq. 1.3 oscillates faster than the fastest Fourier component (black).

Super-oscillatory interference patterns, as in Fig. 1.4, are characterized by a number of relevant parameters (see Fig. 1.5). First, the field of view (FOV), which is determined by the width of the low intensity region around the hotspot. Second, the ratio of the hotspot and sideband intensities, which is an indication of how well the SOL is focusing the light to the hotspot. Third, the backgroud 'grass level' is defined as everything below a certain threshold value, for example 20% of the hotspot intensity. The ratio between this grass level and the

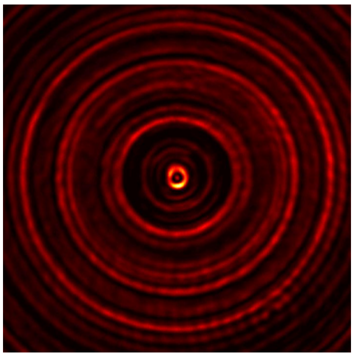

Figure 1.4: The interference pattern of a super-oscillatory lens [10]. In the center the hotspot is visible, surrounded by sidebands.

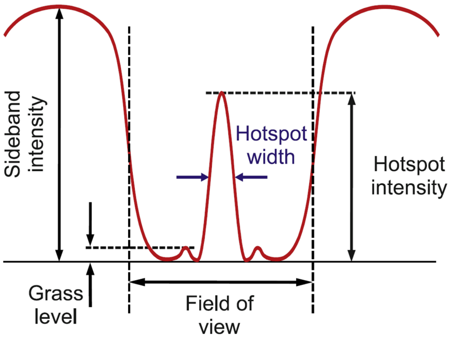

Figure 1.5: Overview of the relevant parameters in the interference pattern of a SOL [11]. The hotspot and sidebands are separated by a darker region, which defines the field of view.

hotspot intensity provides a measure of the noise level [11].

The first experimental proof of lensing via super-oscillations was in 2007 by Huang et al. [9], who focused visible light (500 nm) into very small spots with a quasi-periodic array of nanoholes (see Fig. 1.6 and Fig. 1.7). Their results showed that the smaller the size of the hotspot, the lower the intensity of that hotspot.

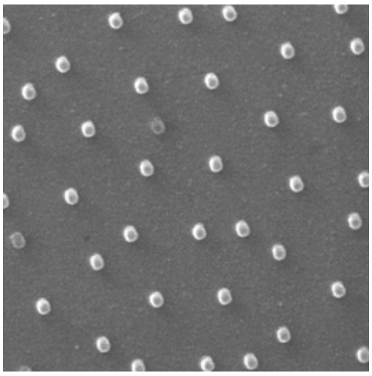

Figure 1.6: SEM picture of the quasi-periodic array of nanoholes used by Huang et al. [9].

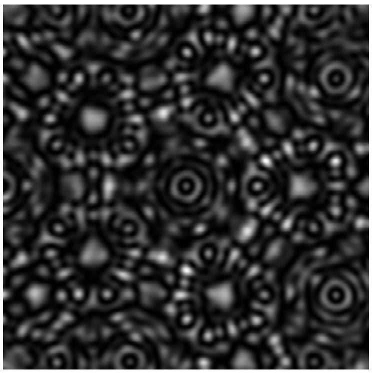

Figure 1.7: Interference pattern observed after transmission of light through the hole array in Fig. 1.6 [9]. At some positions one can see a very small hotspot surrounded by sidebands.

Later, lenses based on a binary amplitude mask consisting of concentric rings (as pictured in Fig. 1.8) were produced and studied by Rogers et al. [7]. Their SOL has a focal distance of 10.3 μm for light at a wavelength of 640 nm when used as an immersion lens. They illuminated an object with the SOL and collected the light with a conventional high NA objective lens to create a super-resolution image. They first used a double slit as a test object, and a Rayleigh resolution better than 0.22λ was obtained, while a diffraction limited high NA lens could only get a 0.63λ resolution (Eq. 1.1). Second, they showed results of imaging a metal film with nanoholes (as shown in Fig. 1.9 and Fig. 1.10), and they obtained a resolution better than 0.17λ. These experiments show that it is possible to use a SOL to illuminate an object and create a super-resolution image.

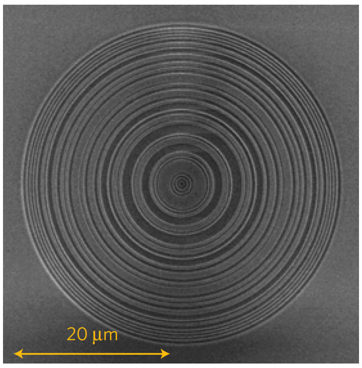

Figure 1.8: SEM image of the SOL with its pattern of binary concentric rings etched away from the metal film [7].

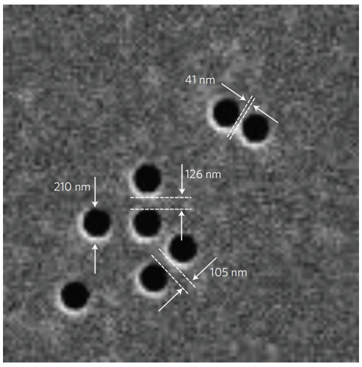

Figure 1.9: SEM image of the subwavelength apertures (210 nm diameter) in a metal film, that were imaged with the SOL from Fig. 1.8 [7].

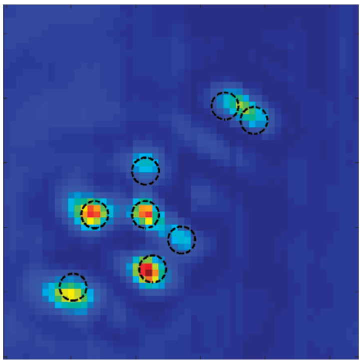

Figure 1.10: The image created by scanning the nanoholes in Fig. 1.9 with the SOL [7]. Most of the holes are resolved, even when they are separated by a distance smaller than the diffraction limit.

One of the disadvantages of a SOL is the presence of sidebands. These limit the field of view and since the sideband intensity is usually (much) higher than the hotspot intensity, scattering light from the sidebands might distort the image [11].

A modification in the binary amplitude mask can partly solve this problem. By blocking the central part of the mask with a 20 μm disc, the sidebands are pushed away from the hotspot, as shown in Fig. 1.11.

The result is an optical needle super-oscillatory lens (ONSOL) that produces a so called “optical needle” in space, as pictured in Fig. 1.12. The diameter of the blocking region determines the length and intensity of the opticle needle formed by the ONSOL. Roy et al. [12], Rogers et al. [10] and Yuan et al. [13] have shown experimentally that an ONSOL can produce a hotspot with a FWHM between 0.38λ and 0.45λ. This is smaller than the diffraction limit, but larger than the SOL hotspot. The length of the optical needle was found to be 10λ to 15λ for these cases.

1.1.1 Theory for this project

The final goal of our project is to investigate the possibility to use a SOL in a confocal setup for super-resolution imaging. This is different from the experiments by Rogers et al. [7], since the collection of the light from the object will be done by the SOL instead of a conventional objective lens. Our goal is to use one SOL for both the illumination of an object and for collecting the light. As a very first step, the performance of our SOL sample is characterized.

Disadvantages of a SOL are the presence of unwanted sidebands, the low intensity of the hotspot compared to the intensity of the sidebands (which results in a low focusing efficiency) and the low transmission because an opaque amplitude mask is used. The intense sidebands make it more difficult to make good images with a SOL, and the low transmission

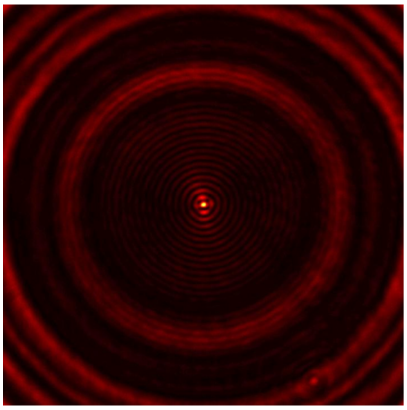

Figure 1.11: The interference pattern of an ONSOL [10]. In the center the hotspot is visible surrounded by sidebands. However, the field of view is much larger than for a SOL (compare with Fig. 1.4).

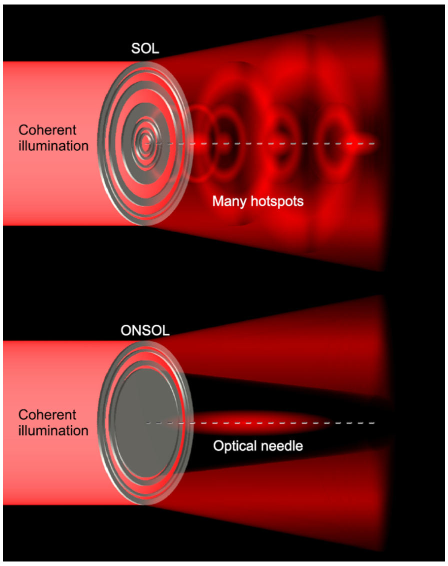

Figure 1.12: Comparison of the interference pattern created by a SOL and an ONSOL [10]. The SOL creates multiple hotspots at different distances from the lens, while the ONSOL creates one hotspot that persists over a longer distance.

and low focusing efficiency require incident light with a very high intensity. Therefore the applicability of SOLs for imaging requires further investigations in terms of image processing.

Design of the SOL mask

The design for our SOL is equal to the design used by Roy et al. [7][12]. The mask was optimized using a binary particle swarm optimization (PSO) method, a ‘nature-inspired evolutionary algorithm for stochastic optimization’ [7]. It is based on the exchange of information between individuals of a population, like bees or starlings. Each member of the population will remember the location with the optimum value on its own trajectory: the personal best [14]. This location is communicated to the other members and the optimum location of the whole swarm is called a global best. In the next step, the trajectories of all members are adapted based on the location of the global best. In this way, the chance to find the global minimum in the optimization process instead of a local one increases.

For the optimization process of the SOL mask, the structure is initially divided into N concentric rings with a transmittance of 0 or 1. The goal of the optimization was to get a FWHM for the central hotspot as small as possible. In addition, we required that the field of view and the side lobe level (see Sec. 1) had values that are experimentally feasible [7]. The 60 particles for the PSO were thus moving in an N-dimensional space to find the optimum combination of open and closed rings in 10000 iterations [7]. In this way, an optimum pattern of rings with a specific width was found that is shown in more detail in the appendix.

Simulations on the SOL

To check how our results relate to theory, we compare them with simulations performed within an on-going PhD project at TNO. The simulations are based on the angular spectrum method (ASM), and were performed to predict the interference pattern created by the SOL, and hence its performance. The ASM is based on scalar theory of diffraction, and uses the propagation of (plane) waves to calculate the field at any position [15].
We assume a plane wave with a Gaussian beam profile incident on the SOL. In Fig. 1.13 the trajectory of light is shown: light is transmitted from air to the glass substrate of the SOL, propagates through the glass, makes the transition from glass to air and subsequently only part of the light is transmitted by the SOL mask. The spectrum of the field ($E_{\Delta z}(f_x, f_y)$) at any position Δz from the SOL is calculated by propagating the spectrum transmitted by the SOL, using the Kirchhoff boundary conditions (for a detailed description, see [15]):

$$E_{\Delta z(f_x,f_y)} = E_{afterSOL}(f_x, f_y) \cdot exp(2\pi i f_z \Delta z) \tag{1.5}$$

with f_{xyz} the spatial frequencies. From the spectrum of the field, the field distribution is calculated by taking the inverse Fourier transform of the spectrum (which is similar to the expression in Eq. 1.4).

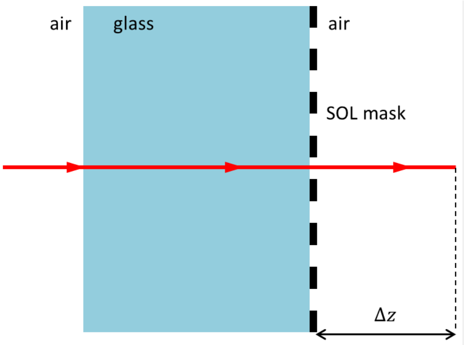

Figure 1.13: Schematic picture of the propagation trajectory of a plane wave through the SOL sample to a distance Δz from the SOL.

1.2 Optical metasurfaces

Compact optical devices are interesting for integrated sensors and on-chip nanophotonic devices. For that purpose, metasurface optical devices are required that are thinner and characterized by smaller working distances than the conventional ones (like lenses, polarizers and waveplates).
An optical metasurface induces an abrupt phase shift upon the light using subwavelength resonators on a dielectric substrate. There are three properties that distinguish metasurface optical devices from conventional ones [16]. First, the phase shift for the incident light is accomplished over a distance of the order of the wavelength. Second, it is possible to design the resonators and thus the wavefront with subwavelength resolution. It has been shown that this property makes it possible to concentrate all incident power into a single useful beam. Third, with metasurfaces one can engineer the interaction of the nanostructures with both the electric and magnetic component of the incident light. [16]

For conventional optical elements, we can describe the path of the light as the shortest way from one point to another, also known as Fermat's principle [1]. The same principle applies to metasurfaces, where we take the extra phase shift $\Phi(\vec{r_s})$ into account that is induced at position $\vec{r_s}$. Fermat's principle can also be stated as the principle of stationary phase, which means that the total phase shift for light propagating from point A to B will be constant for infinitesimal variations of the path [17]. Yu et al. show that this assumption leads to the generalized Snell's law of refraction [17]:

$$n_r sin(\theta_r) - n_i sin(\theta_i) = \frac{\lambda_0}{2\pi}\frac{d\Phi}{dx} \tag{1.6}$$

with $n_{i,r}$ the refractive index of the medium and $\theta_{i,r}$ the angle of incidence and refraction respectively. From this equation, it is clear that the refracted light can be steered in any desired direction by designing the metasurface such that the correct phase shift is applied. In order to shape the planar wavefronts of the incident light into spherical ones with a focus at distance f, the metasurface should impose a phase profile [16]

$$\phi_{lens}(x,y) = \frac{2\pi}{\lambda}\left(f - \sqrt{x^2+y^2+f^2}\right). \tag{1.7}$$

In the paraxial approximation, and assuming $n = 1$, this reduces to:

$$\phi_{lens}(x,y) = \frac{k_0}{2f}\left(x^2+y^2\right). \tag{1.8}$$

In order to operate as an efficient optical device, a metasurface must have a transmission with an amplitude close to 1 and a phase profile with the desired distribution. There are different ways to accomplish this: a dielectric substrate with arrays of either metal or dielectric resonators. Both have been studied by several research groups, and the results will be discussed in the next sections.

1.2.1 Metal resonators

Metasurfaces consisting of arrays of metal resonators (antennas) are based on surface plasmons. The incident light on the antenna is coupled into surface electromagnetic waves, which leads to charge oscillations of the electrons inside the antenna [16]. This phenomenon is known as surface plasmons, which is characteristic for the interaction of metal nanostructures with electromagnetic radiation [3]. Since the nano antennas have a size smaller than the wavelength, the surface plasmons are localized. The desired abrupt phase change of the incident light is the result of a strong interaction of light with localized surface plasmons [3].

Several experiments have been performed on arrays of plasmonic rod antennas by Yu et al. [16][18][17]. They use V-shaped gold optical antennas on a Si substrate (see Fig. 1.14), because those are relatively easy to fabricate and have many tailorable properties like size, shape and orientation. Two unit vectors $\hat{s}$ and $\hat{a}$ are defined for the orientation of a V antenna, $\hat{s}$ along the symmetry axis and $\hat{a}$ perpendicular to it. V-shaped antennas support both symmetric and anti-symmetric modes, that are excited by the components of the electric field along the two axes. When the incident light has an arbitrary polarization, both antenna modes (symmetric and anti-symmetric) are excited. Because they are oriented differently,

the modes are excited with different amplitude and phase, so the polarization of the incident and scattered light can be completely different.
For infrared light, Yu et al. have experimentally demonstrated the generalized laws of reflection and refraction (Eq. 1.6). Fig. 1.15 shows the experimental (circles and triangles) and theoretical (solid lines) results of measurements on ordinary (black) and anomalous (red) refraction. According to their measurements, anomalous refraction by their antenna array occurred for wavelengths between 5 and 10 μm [17].

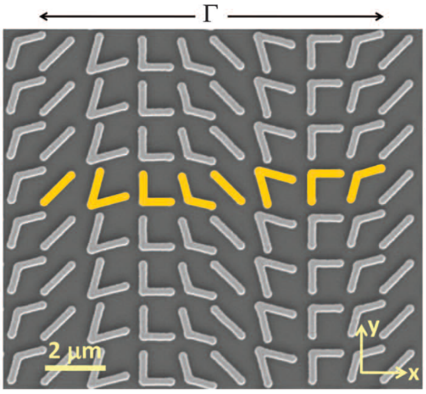

Figure 1.14: Scanning electron microscope (SEM) image of the array of V-shaped gold resonators on a Si substrate [17]. The yellow antennas indicate the unit cell of this array.

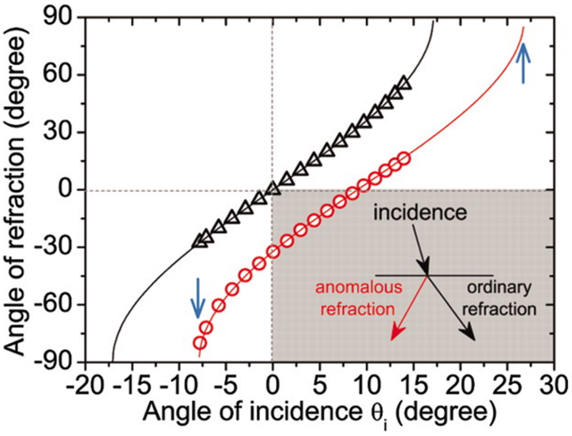

Figure 1.15: The results of experiments (circles and triangles) and simulations (solid lines) for respectively anomalous (red) and ordinary (black) refraction of infrared light by the metasurface in Fig. 1.14 [17].

Ni et al [19] have used a complementary structure: instead of gold nano-antennas on a substrate they use an array of perforated nano-voids in a 30 nm thick gold film (see Fig. 1.16). The nano-voids are V-shaped subwavelength structures that interact with the incident light via surface plasmons.
Lenses with different focal distances were produced for proof-of-concept experiments. Fig. 1.17 shows their results for a metasurface lens with a focus at 5 μm illuminated for visible light of 676 nm. Both the simulations and experiments show that the light can indeed be focused at 5 μm by this type of lens [19].

The biggest problem with metasurfaces consisting of metal resonators are (nonradiative) optical losses [20]. Because of these losses, the transmission efficiency of the metasurface will be low and therefore also the focusing efficiency. In addition to that, part of the incident light is refracted ordinarily [17] and this further reduces the efficiency.

1.2.2 Dielectric resonators

A way to overcome the disadvantage of large optical losses due to the metallic resonators is by using arrays of dielectric resonators. It has been shown that subwavelength dielectric nanoparticles like the ones in Fig. 1.18 scatter the light, and the corresponding electromagnetic field can in first order be described as a superposition of the fields generated by

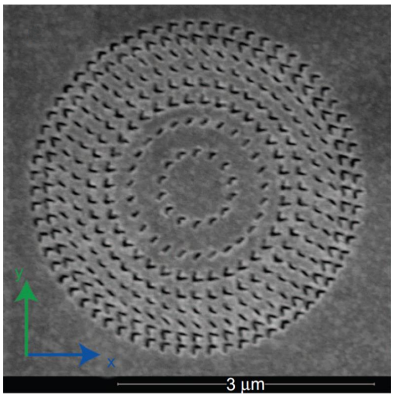

Figure 1.16: SEM image of the perforated V-shaped nano-voids in a gold film used by Ni et al. [19] to manipulate light with a wavelength of 676 nm.

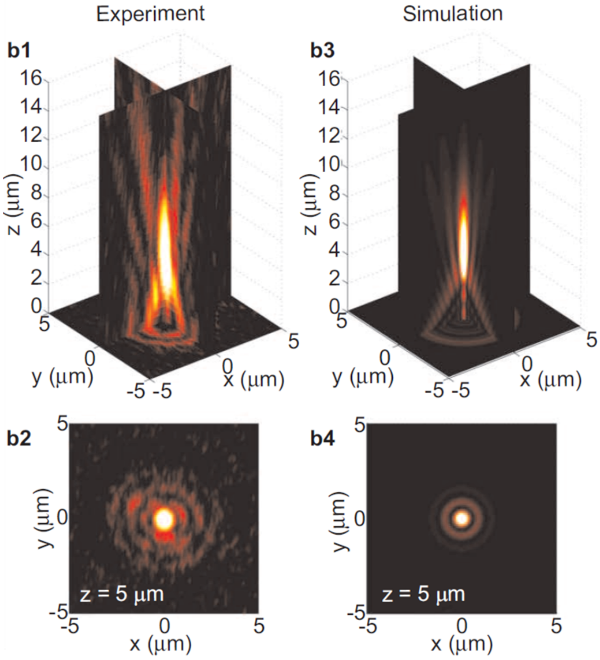

Figure 1.17: Experimental (left) and theoretical (right) results for the beam profile of light after passing through the metasurface in Fig. 1.16 [19].

orthogonal electric and magnetic dipoles in the plane of the resonator (for normally incident light) [3][20][21][22]. An electric dipole can be seen as an alternating current with charges oscillating in one direction in an infinitesimal volume, while a magnetic dipole can be pictured as an alternating current circulating in an infinitesimally small ring. The radiation intensity patterns have the shape of a “horn torus” and neither of the dipoles radiates along its axis. By combining the scattering of both the electric and magnetic resonances, directional scattering can be accomplished [20][23]. If the electric and magnetic modes overlap spectrally (as in Fig. 1.19), the backward scattering is reduced and therefore the transmission is higher. Recently, a number of groups have studied the behaviour of arrays of dielectric devices, mostly with Si cylindrical nanoparticles on a glass or silicondioxide (SiO_2) substrate.

In 2012, Evlyukhin et al. [21] studied individual spherical Si nanoparticles in air with a diameter of 200 nm. The experiments and simulations were performed in the visible regime with wavelengths of 400 to 950 nm. They found that the scattered electromagnetic fields can indeed be described by magnetic and electric dipolar resonators with polarizabilities given by Mie theory. These optical properties demonstrated for single Si resonators can be used for further investigation and design of arrays of resonators.

In contrast to the research of Evlyukhin et al., who worked with visible light, most other groups have investigated optical metasurfaces operating at infrared (IR) wavelengths. Staude et al. [20] fabricated square arrays of disk-shaped Si nanoparticles embedded in SiO_2 and performed measurements in the infrared (0.85 to 2 μm). The results show that the elec-

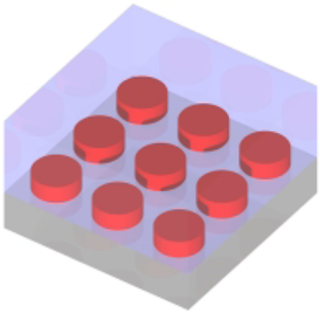

Figure 1.18: Example of subwavelength dielectric nanoparticles embedded in a dielectric medium to create a full-dielectric metasurface [20].

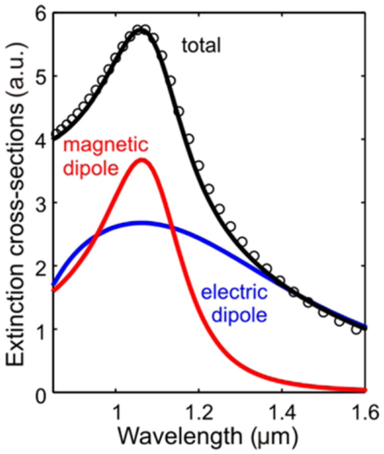

Figure 1.19: The electric, magnetic and total extinction spectra for a single Si nanodisk for the situation where the dipole resonances overlap [20]. The solid lines show the results of discrete dipole approximation, the circles are obtained by finite-integral frequency-domain calculations [20].

tric and magnetic resonances of individual subwavelength Si nanodisks can be spectrally tuned by varying the aspect ratio, which is the ratio between the height and diameter of the nanoparticles. When the resonances are tuned such that they overlap, a high transmission is accomplished.

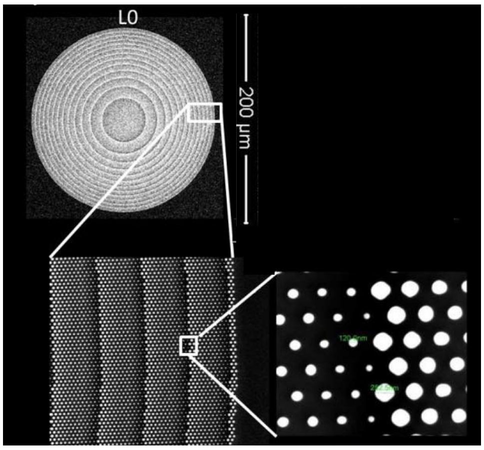

Figure 1.20: SEM images of the hexagonal array of subwavelength Si pillars on a glass substrate used by VO et al. [24].

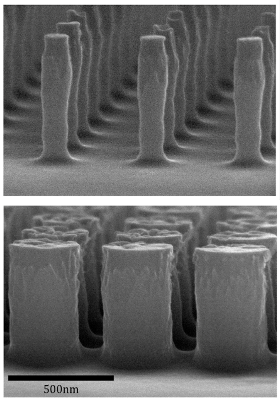

Figure 1.21: SEM images of two square pillar arrays with different pillar diameter but constant periodicity used by West et al. [25].

Vo et al. [24] created hexagonal arrays of cylindrical amorphous Si pillars on a glass substrate, as shown in Fig. 1.20. The goal was to demonstrate a highly efficient, sub-wavelength thick, transmitting focusing element. Therefore they designed and produced multiple lenses with a design wavelength of 850 nm, which impose the phase profile from Eq. 1.8 to create spherical waves so the light is focused at distance f from the lens. As for conventional lenses, a Gaussian shaped intensity distribution was observed. The overall efficiency (approximately 70%) is lower than the theoretical value due to optical scattering as a result of random fluctuations in the nanopost diameters.

The metasurface lens of Vo et al. from Fig. 1.20 creates a phase mask to focus the incident light. Also West et al. [25] are using arrays of Si pillars as a phase mask, as shown in Fig. 1.21. But their arrays are square instead of hexagonal and the design wavelength is 1550 nm. They chose to vary the pillar diameter to create spatial variations in effective refractive index of the metasurface, because pillars with larger diameter result in a higher volumetric fill factor if the periodicity of the pillars is constant throughout the array. This will give a higher effective refractive index and the incident light accumulates a larger phase difference. With this type of lenses, they investigated the beam profile at different distances from the lens. Their results show a focal distance of less than 500 μm, and the full width half maximum (FWHM) of the incident beam is a factor three smaller in the focus. With this, they show that the array is focusing the light. However, the spotsize in focus is still much larger than for a conventional lens.

In 2015, Arbabi et al. [26] published the results of their polarization insensitive metasurface lenses operating at 1550 nm. These lenses are able to focus the light to a spot with a FWHM of 0.57λ (see Fig. 1.22), just above the diffraction limit. To accomplish this, they produced hexagonal and square lattices with high-index Si posts on a low-index SiO_2 substrate. Different designs were applied to realize different focal distances for the same 1550 nm illumination beam. The results show that lenses with a larger focal distance focus the light to a spot with a larger FWHM. In addition, the amplitude of the transmission and the focusing efficiency increase with focal distance. This behavior was also predicted by the full 3D finite difference time domain (FDTD) simulations they performed. Finally, they investigated the functionality of the lens for wavelengths other than the design wavelength. They found that for shorter wavelengths (1450 nm instead of 1550 nm), the FWHM spotsize increases with 0.2λ and the focusing efficiency decreases with 15%.

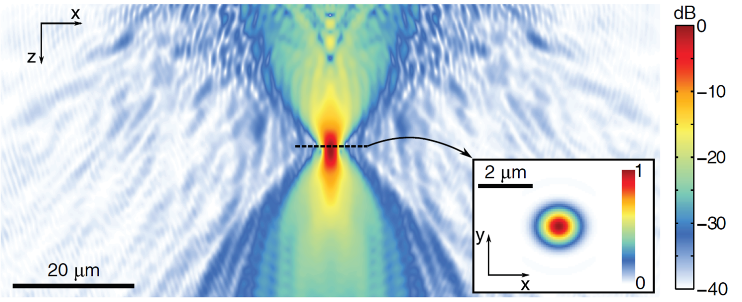

Figure 1.22: Energy density in the xz-plane obtained by full 3D finite difference time domain (FDTD) simulations for an array of Si posts[26]. The inset shows the 2D intensity profile in the focal plane.

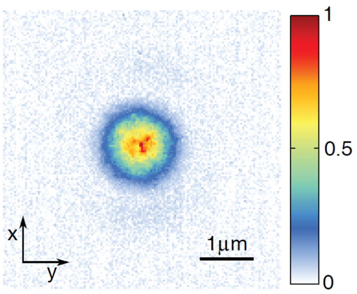

Figure 1.23: Experimental result of the 2D intensity profile in the focal plane of a similar lens as in Fig. 1.22 [26].

Most metasurface lenses are designed for a specific wavelength and perform differently for

other wavelengths. Therefore, optical metasurfaces will suffer from chromatic aberrations due to the wavelength dependence of the refractive index, just like conventional optics [1]. In addition to that, chromatic aberrations are also caused by the dimensions of the array. For light with a larger wavelength than the design wavelength, the effective size of the resonators (r_{res}/λ) and the effective distance between the resonators (a/λ) is smaller. This also influences the field scattered by a resonator, and thus induces chromatic aberrations.
Aieta et al. [27] have presented a way to deal with this problem by using the engineered wavelength dependent phase shift that can be imposed by a metasurface. The total accumulated phase consists of two contributions, one by the metasurface itself and one due to propagation:

$$\phi_{total}(r,\lambda) = \phi_{metasurface}(r,\lambda) + \phi_{propagation}(r,\lambda). \tag{1.9}$$

To remove chromatic aberration, ϕ_{total} should be constant for different wavelengths. This can for example be achieved by requiring that $\phi_{metasurface}(r,\lambda) = -\phi_{propagation}(r,\lambda) = -\frac{2\pi}{\lambda}l(r)$ to compensate for the propagation phase shift. Aieta et al. demonstrate this principle with a metasurface that deflects three wavelengths (1300 nm, 1550 nm and 1800 nm) at the same angle. Simulations show that the same principle can be used to design an achromatic flat lens with the same focal distance for the three design wavelengths. However, the other wavelengths will still be focused at a different distance.

In conclusion, previous experiments have shown that metasurfaces with either metal or dielectric resonators can act as a lens for different wavelengths in the infrared and visible regime. They can focus the light into a spot with a FWHM close to the diffraction limit, for focal distances of the order of 100λ. However, considering the transmission, dielectric resonators are a better choice.

1.2.3 Theory for this project

The optical metasurfaces used for our experiments consist of subwavelength cylindrical Si resonators embedded in a SiO_2 substrate (see Fig. 1.24). As explained before, the field scattered by subwavelength resonators can in first order be described in terms of electric and magnetic dipoles. It has been shown that the resonance wavelength of the dipole can be tuned by tailoring the properties of the sample, such as the refractive indices of the resonators and embedding medium, and the height and radius of the resonators. If the two dipoles resonate at the same wavelength, almost unity transmittance of the incident field is reached, which is necessary to create efficient optical metasurfaces.

Dielectric resonators to focus the light

To focus light like a conventional lens, the optical metasurface consists of an array of cylindrical Si resonators with periodicity a (see Fig. 1.25). In order to create a focus, the metasurface has to impose the phase profile $\phi_{lens}(x,y) = \frac{k_0}{2f}\left(x^2+y^2\right)$ from Eq. 1.8 onto the incident light. Since the metasurface is extremely thin (order of the wavelength), this phase profile is realized by the resonators.
To accomplish this, first a single unit cell (as in Fig. 1.24) is simulated in the commercially available finite element software HFSS [28]. The unit cell was assumed to be in an infinite array of equal cells. A multi-step parameter analysis has been performed for the following parameters: the height of the Si cylinders h_c, the total height of the embedding SiO_2 h_{emb},

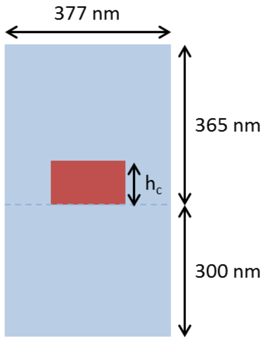

Figure 1.24: Schematic cross section of a unit cell from the array of cylindrical Si resonators (red) embedded in a SiO$_2$ substrate (blue).

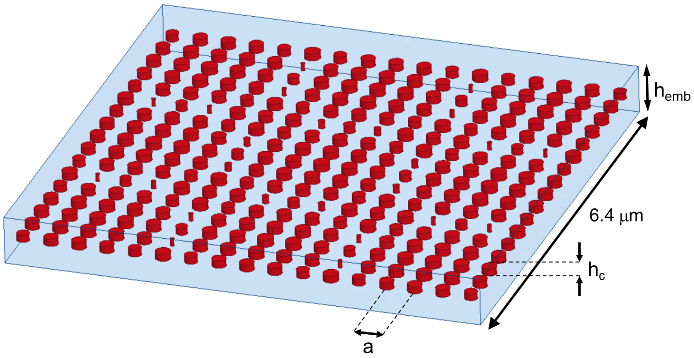

Figure 1.25: Schematic picture of an array of 17x17 cylindrical Si resonators (6.4x6.4 μm^2) embedded in a SiO$_2$ substrate with thickness h_{emb} [22]. The lattice constant of the array is $a = 377$ nm and the height of the cylinders is indicated with h_c. The diameter of the cylinders is varying, such that the desired (parabolic) phase profile will be imposed and this metasurface will work as a lens.

the height in the SiO$_2$ at which the resonators are embedded h_{inf}, the radius of the resonators r and the periodicity a of the medium [28].

By this analysis, the optimum values of the parameters were chosen to obtain an almost unit transmission and a small transmission variation as a function of resonator radius r. By relatively small variations in r one obtains the plots from Fig. 1.26. These plots show that the phase of the field that is scattered by the resonator depends on the radius of that resonator.

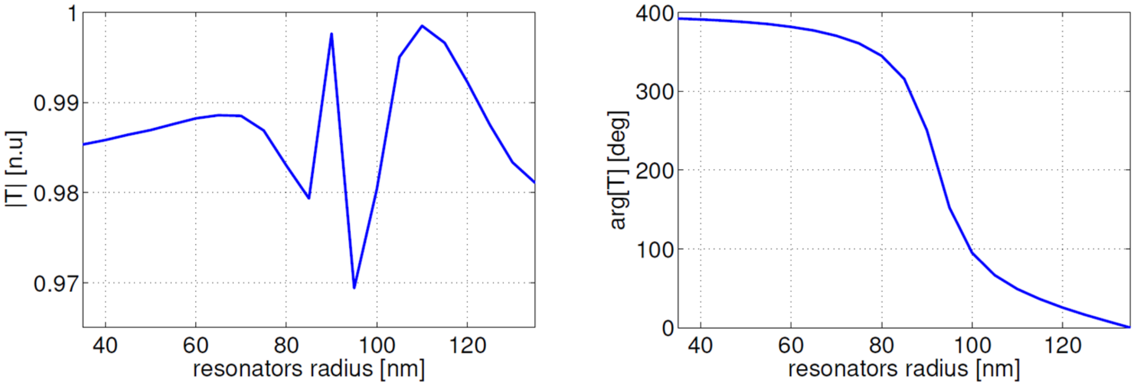

Figure 1.26: Graphs of the magnitude (|T|) and the phase (arg(T)) of light scattered by a single Si cylindrical resonator as a function of the resonator radius.

From the desired parabolic phase profile we know what phase the field scattered by each resonator should have. Together with the phase information from Fig. 1.26 this indicates what radius each resonator in the array should have. As an example, Fig. 1.25 shows a schematic representation of 17x17 resonators with varying radius that is designed to impose a parabolic phase profile and focus the light. This array contains mirror symmetry in x, y and 45°.

To verify whether this surface indeed focuses the light at a focal distance f, HFSS simulations were performed with a Gaussian beam (635 nm, beam waist radius 3λ) incident on a finite array with the following design parameters: 17x17 resonators (6.4x6.4 μm^2), $f = 3\lambda = 1.9$ μm, $a = 377$ nm, $h_{emb} = 665$ nm, $h_{inf} = 300$ nm, $h_c = 96$ nm, $n_{Si} = 3.87$ and $n_{SiO_2} = 1.5$. With a lens size of $L_{lens} = 6.4$ μm and $f = 1.9$ μm in air ($n = 1$), we can calculate the NA that is expected for a diffraction limited lens with these dimensions:

$$\text{NA} = nsin\left[tan^{-1}(L_{lens}/2f)\right] = 0.86. \tag{1.10}$$

An NA of 0.86 means that the FWHM of an Airy pattern (Eq. 2.3) is approximately 0.59λ.

Fig. 1.27 shows the simulated xz intensity distribution as a function of the distance z from the metasurface, where $z = 0$ is defined in the plane of the resonators. The focus is expected at 1.9 μm, which is indicated in the figure with the white dotted line. The figure shows that the light is indeed focused to a single spot, but according to the simulations, the focus is located closer to the metasurface than designed. Fig. 1.27 is the xy intensity distribution in the plane indicated by the white line from Fig. 1.28. The FWHM of this spot is approximately 1.2λ, which is much larger than the 0.59λ of a diffraction limited lens with the same dimensions.

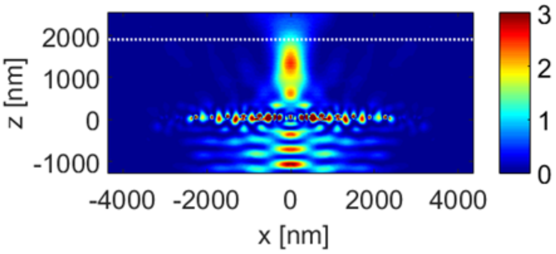

Figure 1.27: Intensity distribution as a function of the distance z from the surface of the optical metasurface, obtained with HFSS simulations of a finite array of 17x17 resonators as in Fig. 1.25 [22]. A line at $3\lambda = 1.9$ μm from the plane of the resonators indicates where the focus is expected according to the design of the lens.

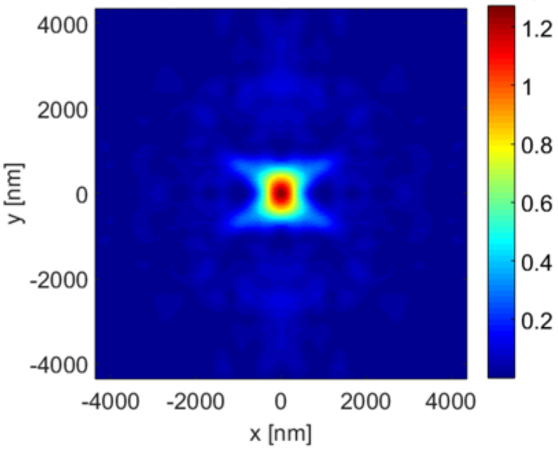

Figure 1.28: The intensity distribution ($|E(x,y)|^2$) in the plane that is indicated with the white line in Fig. 1.27, obtained with HFSS simulations of a finite array of 17x17 resonators as in Fig. 1.25 [22].

Dielectric resonators to influence the polarization

Steering of light with a metasurface is interesting to make superthin high NA lenses, but there are more possibilities. If it is possible to change the polarization of the incident light, one can also design metasurface polarizers, polarization scramblers and waveplates. For our experiments, we designed and manufactured some metasurfaces that operate as a quarter waveplate and some polarization scramblers.

When a subwavelength dielectric resonator is illuminated with linearly polarized light, the electric dipole will have the orientation of the incident light while the magnetic dipole is oriented orthogonal to that. If the resonator has a circular cross section as in the previous section, it is symmetric and the scattered field will have the same polarization as the incident field. However, in the case of an elliptical cross section, the symmetry is broken and the scattered field might have a different polarization. Fig. 1.29 shows the situation for an elliptical resonator at an angle of 45° with respect to the incident field E_{inc}. The field can be decomposed into two equal components along the principal axes of the ellipse: $E_{||}$ and $E_{\perp}$. Since the size of the resonator is different along these axes, the $E_{||}$ and $E_{\perp}$ components of the field scattered by this resonator will be different. Therefore the polarization of the scattered field is different from the incident field.

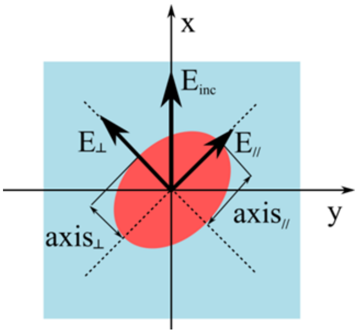

Figure 1.29: Schematical cross section of an elliptical Si resonator embedded in SiO_2 oriented at 45° with respect to the incident field E_{inc} along x. The incident field is decomposed into its two components along the principal axes of the ellipse.

The design procedure was similar to the one for the metasurface lenses. HFSS was used to simulate an infinite array of elliptical resonators with periodicity a. Next, the optimum parameters were estimated to obtain a maximum transmission. In order to create a quarter waveplate, the fields $E_{||}$ and $E_{\perp}$ should have equal amplitude but a $\pi/2$ phase difference. By tuning the ratio between the long and short axis of the elliptical resonators, the optimum value can be found. For this array, all resonators have the same dimensions and orientation.

The second application of the elliptical resonators is a polarization scrambler. In order to accomplish depolarization of the light, every resonator should scatter the incident light with a different polarization than the other resonators. One way to achieve this is by varying the orientation of the elliptical resonators with respect to the incident polarization. If all resonators have the same axes but a different angle, the ratio of $E_{||}$ and $E_{\perp}$ will be different. Therefore each resonator scatters the light with a different polarization, and the whole array will (partly) depolarize the incident light.

Chapter 2

Materials and methods

The goal of the experiments was to study the performance of a super-oscillatory lens (SOL) and multiple optical metasurfaces. In this chapter, we describe our samples and the methods that were used to design and produce these samples, to image the beam profile created by our samples and to extract information from these images. In addition, a short description is included about the simulations that were performed to provide a theoretical prediction of the performance of both the SOL and the optical metasurfaces.

2.1 SOL

2.1.1 Sample

A SOL is a binary amplitude mask consisting of concentric rings. Our SOL was produced in collaboration with the Else Kooi lab in Delft and is based on a 100 nm titanium film, deposited onto a 3x3 mm^2 dielectric substrate (700 μm glass). The metal film is opaque for the design wavelength of 635 nm. Subwavelength concentric rings are created with electron beam lithography (EBL), followed by etching of the titanium layer to obtain the binary structure as shown in Fig. 2.1 with a total diameter of 40 μm. The diameter and width of the rings vary, and the exact dimensions can be found in the appendix.

2.1.2 Setup

To study the beam profile of light transmitted by the SOL, we built a setup as shown schematically in Fig. 2.3. Light from a laser diode (Thorlabs LP635-SF8, 635 nm) is collimated by a fiber collimator (Thorlabs CFC-5X-A) to a beam with a diameter of 0.87 mm. The light passing through the SOL, which is mounted on an xyz-translation stage (Thorlabs MAX311D/M with closed-loop piezos), is collected by a conventional high NA objective lens (Nikon M Plan Apochromat, 150x, NA 0.95, working distance $wd = 200$ μm). A tube lens (lens 2, Thorlabs, $f = 20$ cm) focuses the light onto a CMOS camera (Allied Vision Manta G-235B) to create a magnified image of the beam profile.

A conventional high NA objective lens can image the hotspot with a spotsize below the diffraction limit, because the hotspot is created by interference of propagating waves. These waves can be collected by a conventional lens.

Measurements were performed by moving the SOL with the piezo stage in z (along the optical axis, see Fig. 2.3) with respect to the objective lens. Steps of 100 nm were made with a

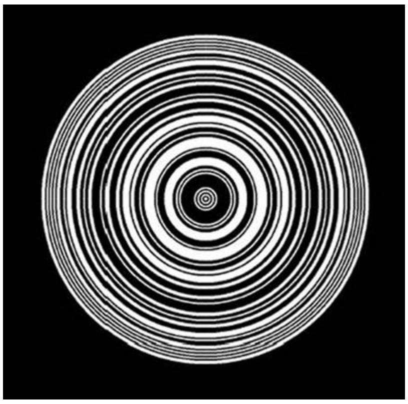

Figure 2.1: Schematic picture of the SOL structure with a diameter of 40 μm, consisting of binary concentric rings. In this picture, black corresponds to the opaque titanium film, white are the regions where the titanium was etched away.

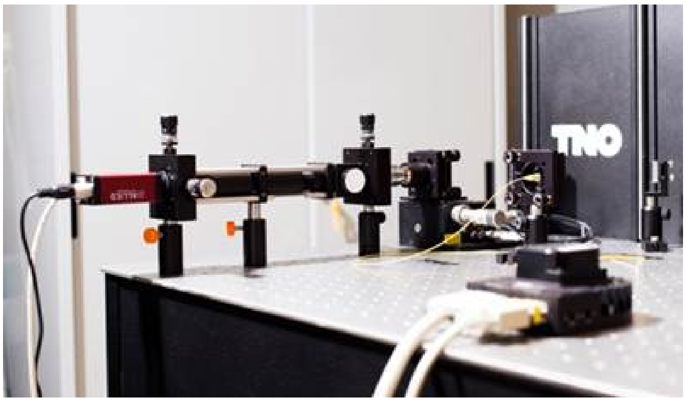

Figure 2.2: Picture of the setup that is shown schematically in Fig. 2.3, that is used to characterize the intensity profile of light transmitted by the SOL.

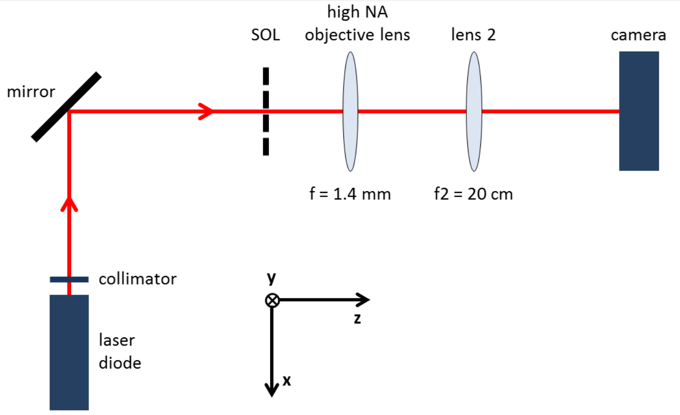

Figure 2.3: Schematic picture of the setup that was used to study the beam profile of light transmitted by the SOL. Light of 635 nm from the laser diode is collimated and directed towards the SOL. The beam profile is imaged with a microscope consisting of a high NA objective lens (lens 1), a tube lens (lens 2) and a CMOS camera.

resolution of 5 nm. An image of the beam profile was recorded after each step.

To determine the position of the focus of the SOL, we need a measure of the distance between the SOL surface and the position where a measurement is performed. To accomplish that, a 50:50 beamsplitter (BS) is inserted in between the objective lens and the tube lens in Fig. 2.3 as shown in Fig. 2.4. A white light source is used to illuminate the SOL via the BS and objective lens. The light is reflected from the sample and the SOL is imaged with the two lenses and the camera. In this way, we can find the position where a sharp image of the SOL surface is obtained. By using this as a reference, we know at each position what the distance to the SOL is.

2.1.3 Data analysis

The measurements yield series of images of the interference pattern created by the SOL, containing a hotspot and many sidebands (as explained in Sec. 1.1). The center of the image consists of the hotspot and a low intensity region surrounding it (the FOV). To characterize the hotspot, a 2D Gaussian was fitted to the FOV in the images:

$$I(x,y) = I_{max}\, exp\left(\frac{-(x-x_0)^2}{2\sigma_x^2} + \frac{-(y-y_0)^2}{2\sigma_y^2}\right) + I_{offset}. \tag{2.1}$$

In this equation, I_{max} is the maximum intensity, (x_0, y_0) the position of the hotspot center, σ_x and σ_y the standard deviations in x and y and I_{offset} an intensity offset due to the background signal. Eq. 2.1 was fitted to the hotspot region with a least-squares fitting function in Matlab, and Fig. 2.5 shows the result of such a fitting procedure. In this figure, the blue dots correspond to the measured hotspot and the colored surface shows the 2D Gaussian fit. Errors for the fitting are estimated with the 95% confidence intervals of the least squares fitting procedure, and will be used for errorbars in the figures.
The most important parameter for us is the full-width-half-maximum (FWHM) of the hotspot, which is calculated from the standard deviation σ via

$$FWHM = 2\sqrt{2\,ln(2)}\,\sigma \approx 2.35\sigma. \tag{2.2}$$

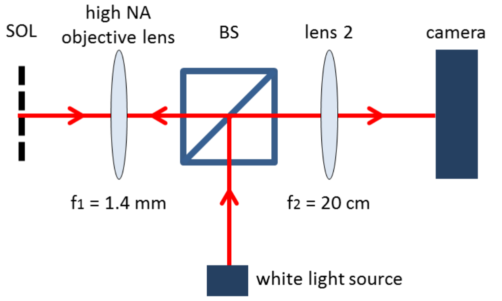

Figure 2.4: Schematic picture of the setup as it is used to determine the distance to the SOL surface. A white light source illuminates the SOL via a 50:50 BS. The light reflected by the SOL is imaged with the two lenses and the CMOS camera.

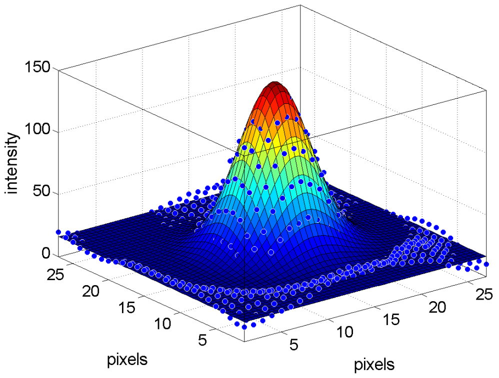

Figure 2.5: Central part of the interference pattern created by the SOL, with the hotspot (blue dots) and a 2D Gaussian fitted to it (colored surface).

2.2 Optical metasurfaces

2.2.1 Sample

The optical metasurfaces for our experiments consist of subwavelength dielectric Si resonators (n = 3.87) embedded in a dielectric SiO_2 substrate (n = 1.5). The production starts with a silicon on insulator (SOI) wafer of 510-540 μm thickness. The top Si layer is partly etched away using reactive ion etching (RIE) to create a regular array of cylindrical Si resonators. Subsequently, another layer of SiO_2 is deposited via plasma-enhanced chemical vapor deposition (PECVD) so the total thickness of SiO_2 becomes 665 nm, as was visualized schematically in Fig. 1.24 in Sec. 1.2.3. In the final production step, the backside of the SOI wafer is etched away using deep reactive ion etching (DRIE) in 1x1 mm^2 regions around the arrays so only the 665 nm thick membrane remains. These areas are the "windows" in the wafer visible in Fig. 2.6. This process is visualized schematically in appendix 6.2.

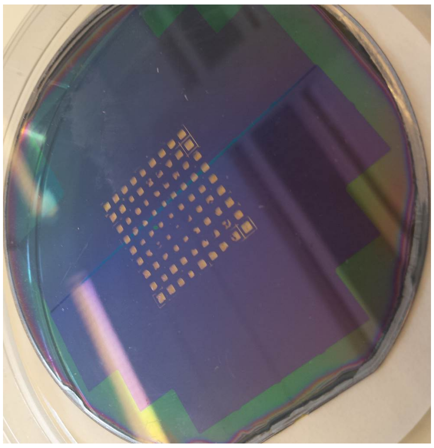

Figure 2.6: Picture of the processed SOI wafer with 81 windows of 1x1 mm^2 and 665 nm thick.

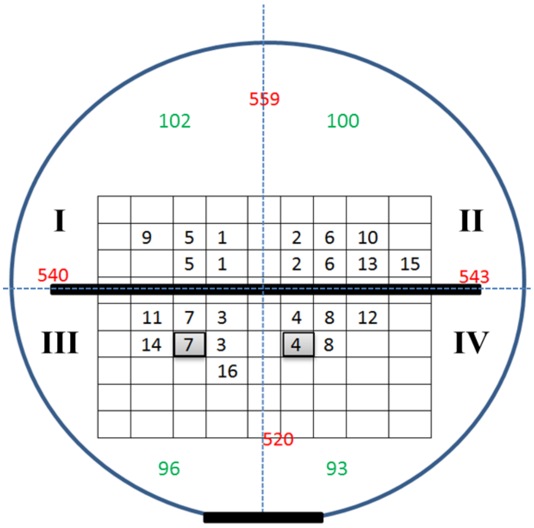

Figure 2.7: Map of the wafer indicating in what window each design is patterned. The four quadrants of the wafer are indicated, as well as the corresponding value of the refractive index (green numbers).

The wafer is divided into four sections (see Fig. 2.7). Each of these quadrants is designed for different tolerances of the wafer refractive index, by varying the height of the cylinders according to four different refractive index values, with quadrant III being the nominal one ($n_{Si} = 3.87$).

On the wafer, 22 windows are patterned with 16 different designs, as is shown in Fig. 2.7. Detailed information about these designs can be found in appendix 6.2. Most important is that design #1 to #8 are all designed to work as a lens, but design #1 to #4 consist of 120x120 resonators while #5 to #8 consist of only 17x17 resonators. Design #9 to #14 are designed to work as a quarter waveplate and design #15 and #16 as a polarization scrambler.

2.2.2 Setup

The setup to perform measurements on the optical metasurfaces is very similar to the one for the SOL (see Sec. 2.1). Light from a laser diode (Thorlabs LP635-SF8, 635 nm) is collimated by a fiber collimator (Thorlabs CFC-5X-A) to a beam with a diameter of 0.87 mm. The light passing through the sample, which is mounted on an xyz-translation stage (Thorlabs MAX311D/M with closed-loop piezos), is collected by a conventional high NA objective lens (Nikon M Plan Apochromat, 150x, NA 0.95, working distance $d = 200\mu$m). A tube lens (Thorlabs, $f = 20$ cm) focuses the light onto a CMOS camera (Allied Vision Manta G-235B) to create a magnified image of the beam profile.
In addition to this, there is the possibility to insert polarizing beamsplitters (PBS) and a waveplate in the setup to investigate polarization effects. The first PBS makes sure that the incident light is linearly polarized along the x or y axis. With a quarter-waveplate (QWP) or a half-waveplate (HWP) in a rotation mount (Thorlabs CRM1), we can manipulate the polarization of the light incident on the sample. The second PBS is also mounted in a rotation mount, and by rotating it we can study the polarization of the light transmitted by the optical metasurfaces, since a PBS can be used as a polarizer.

As for the SOL, the optical metasurfaces were displaced along the z direction, and the transmitted light was recorded with the CMOS camera. The distance to the surface was found as explained in Sec. 2.1.

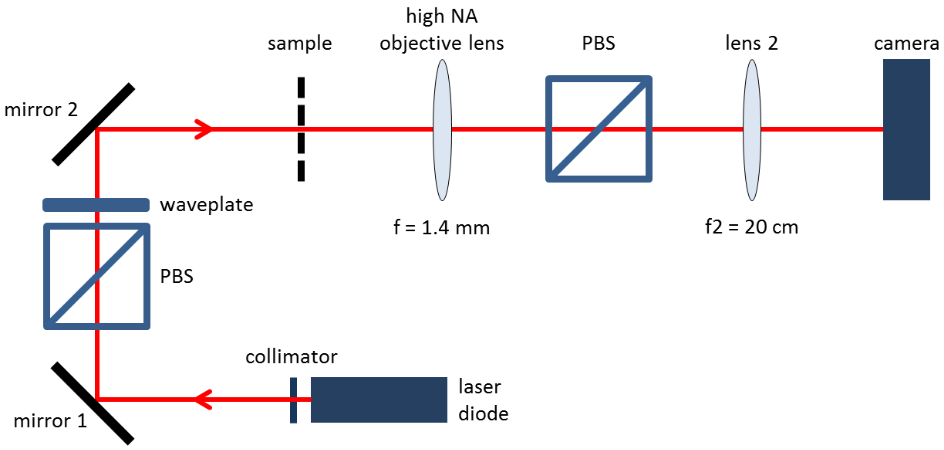

Figure 2.8: Schematic picture of the setup that was used to study the beam profile of light transmitted by the optical metasurfaces. Light of 635 nm from the laser diode is collimated and directed towards the sample. The beam profile is imaged with a microscope consisting of a high NA objective lens, a tube lens and a CMOS camera. To study polarization effects, PBSs and waveplates ($\lambda/2$ or$\lambda/4$) can be inserted.

2.2.3 Data analysis

The measurements yield series of images of the interference pattern created by the optical

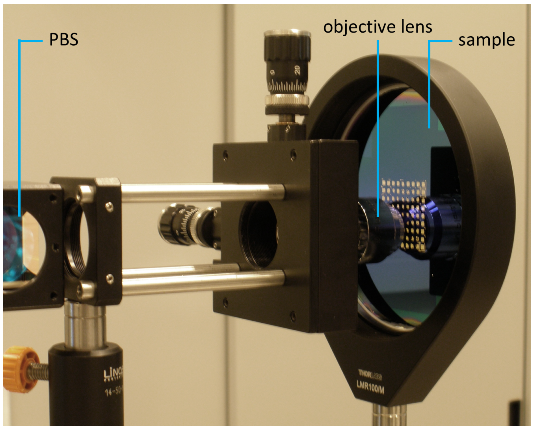

Figure 2.9: Picture of part of the setup from Fig. 2.8, with the sample, objective lens and one PBS.

metasurfaces. For the samples that are designed to work as a lens, we first fitted a 2D Gaussian to the central spot (see Eq. 2.1) to obtain more information about the FWHM and the intensity of the spot. To compare the spot in the focus of these lenses with that of a conventional lens, we can fit an Airy pattern [1] to a line profile of the focal spot

$$I = I(0)\left[\frac{2J_1(2\pi \mathrm{NA}x/\lambda)}{2\pi \mathrm{NA}x/\lambda}\right]^2 \tag{2.3}$$

with I_0 the maximum intensity, J_1 the first order Bessel function of the first kind, NA the numerical aperture of the metasurface lens, x the distance in the xy-plane and λ the wavelength of the incident light. The fit of Eq. 2.3 provides information about the effective NA of the lens.
Errors for the fitting are estimated with the 95% confidence intervals of the least squares fitting procedure, and will be used for errorbars in the figures.

As a final check of the focusing behavior of the metasurface lenses, we can fit a parabola to the graph of FWHM as a function of z. The beam waist $w(z)$ of a Gaussian beam focused by a conventional lens is described by:

$$w(z) = w_0\sqrt{1+\left(\frac{z}{z_R}\right)^2} \approx w_0\left[1+\frac{1}{2}\left(\frac{z}{z_R}\right)^2\right] \tag{2.4}$$

with w_0 the beam waist at the plane of the lens, z the distance from the lens and z_R the Rayleigh length $z_R = \pi n w_0^2/\lambda_0$. The approximation is true for $z/z_R \ll 1$, which is the case for the laser beam used in our experiments. We can see on the right hand side of Eq. 2.4 that the waist of the beam should have a parabolic dependence on z.

Chapter 3

Results from the SOL

3.1 Characterization of the SOL

For imaging experiments with the SOL it is important to know more about the performance of the SOL. Therefore we characterized the interference pattern created when the SOL is illuminated with plane waves. This section contains results of those measurements and a comparison with simulations.

3.1.1 Experimental results

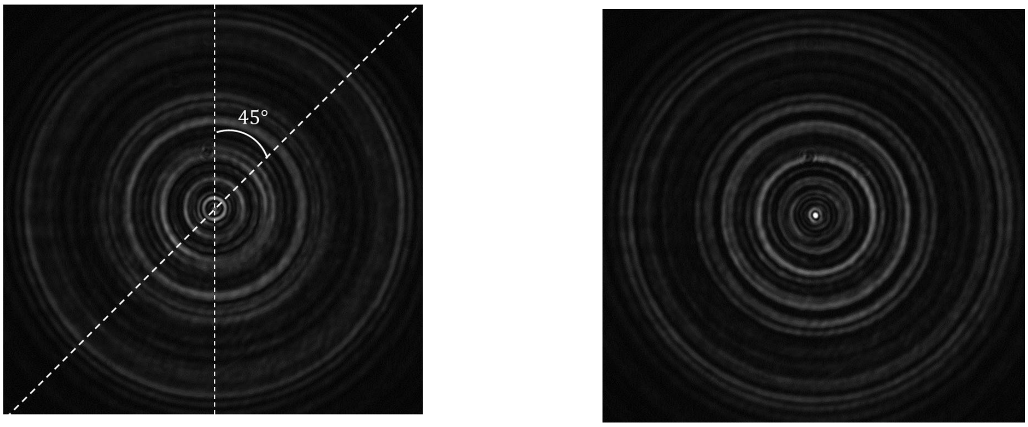

(a) (b)

Figure 3.1: Beam profiles taken with the CMOS camera of two different distances z between the objective lens and SOL surface. The intensity of the hotspot varies with z, as well as the intensity and the position of the sidebands. In (a) the line at an angle of 45° is shown at which the line profiles were taken to create Fig. 3.7.

With the setup as described in Sec. 2.1 we imaged the beam profile of light transmitted by the SOL while scanning in z (along the optical axis of the system). Two examples of such beam profiles are shown in Fig. 3.1a and Fig. 3.1b. For all images in this chapter, $z = 0$ is defined as the plane of the SOL and the light is propagating in the $+z$ direction.

By combining cross sections through the center along x or y for all beam profiles, xz and yz

intensity profiles were created. The results are shown in Fig. 3.2a and Fig. 3.2b respectively, where z is the distance from the SOL surface to the position where the corresponding image was taken. Because of the rotational symmetry of the SOL, we expect the xz and yz intensity profiles to be similar, which they are. Both figures show that the the intensity of the hotspot and the intensity and position of the sidebands vary with z. Moreover, they suggest that the smallest spotsize is obtained when the hotspot intensity is the lowest.

To confirm this relation, the central part of each beam profile image (which contains only the hotspot and the darker area surrounding it) was fitted with a 2D Gaussian (Eq. 2.1), as was demonstrated in Fig. 2.5. The thus obtained fit parameters provide a measure of the FWHM of the hotspot and its maximum intensity as a function of z, which is displayed in Fig. 3.3 and Fig. 3.4 respectively. We can see that the intensity is minimal for the hotspot with the smallest FWHM. In Fig. 3.4, also the FWHM of the focus of a diffraction limited lens with high NA is indicated ($\lambda/(2\text{NA}$, assume NA ≈ 1). The spotsize of the SOL is smaller than the diffraction limit in the range $5.2 < z < 6.2$ μm.

At $z = 5.4$ μm we measured $\text{FWHM}_x = 0.38 \pm 0.03\lambda$ and $\text{FWHM}_y = 0.34 \pm 0.03\lambda$. This position is called the focus of the SOL, since this is the smallest measured FWHM of the hotspot.

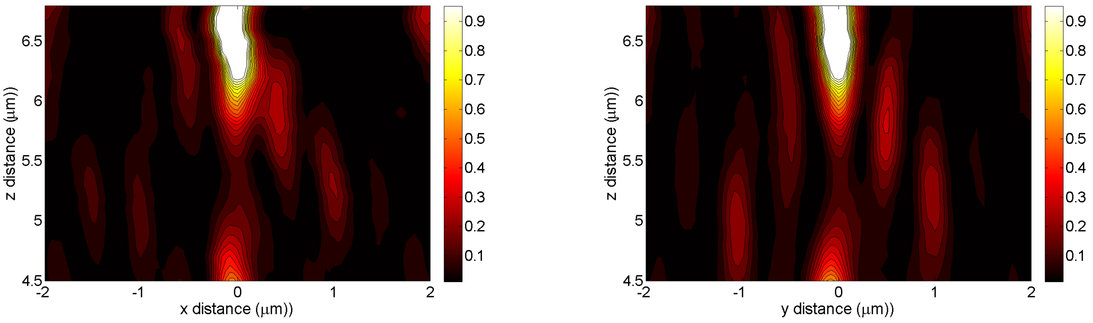

(a) (b)

Figure 3.2: Intensity profiles in xz (a) and yz (b) that show the intensity and position of the hotspot and sidebands in the interference created by the SOL. For these images, $z = 0$ is defined as the plane of the SOL and the light is propagating in the $+z$ direction.

3.1.2 Comparison with simulations

To check to what extent the SOL is performing as expected, we compare the data with ASM simulations (see Sec. 1.1.1).

The intensity profile in Fig. 3.5 is the simulated equivalent of the profile in Fig. 3.2a and Fig. 3.2b. Fig. 3.6 shows the calculated spotsize between 5 and 6 μm from the SOL surface (blue) in comparison with the experimental values (black) from Fig. 3.4. Here we see that the trend in the spotsize as a function of z is similar for the experimental results and the simulations.

By comparing Fig. 3.2b and Fig. 3.5 we observe similarities in the relative position and intensity of the sidebands. To take a closer look, line profiles are made in the focal plane of the simulated and measured beam profiles (as the ones in Fig. 3.1), and plotted in Fig. 3.7.

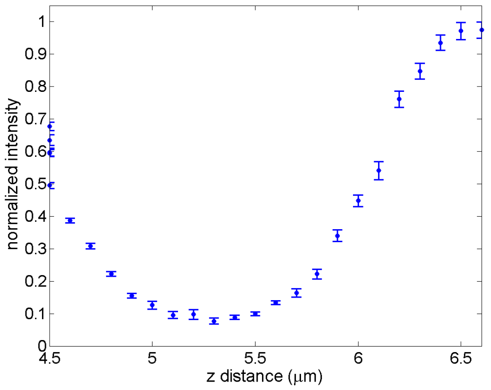

Figure 3.3: The (normalized) intensity of the hotspot as a function of distance from the SOL surface, obtained by fitting a 2D Gaussian to the hotspot images.

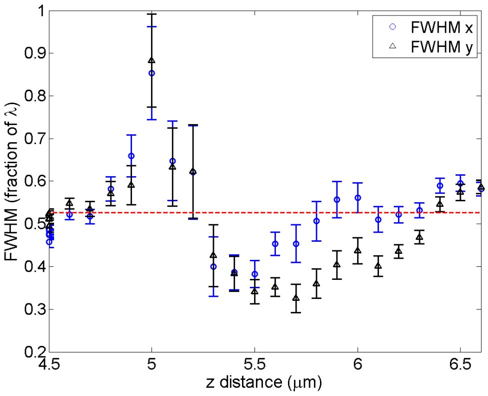

Figure 3.4: The FWHM of the hotspot as a function of distance from the SOL surface, obtained by fitting a 2D Gaussian to the hotspot images. The calculated spotsize of a diffraction limited lens is indicated with the red dotted line.

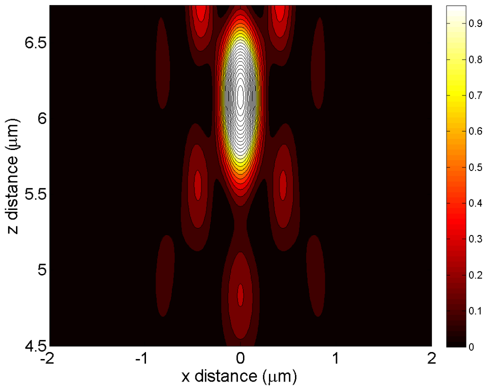

Figure 3.5: Intensity profile showing the results of ASM simulations of the SOLs performance.

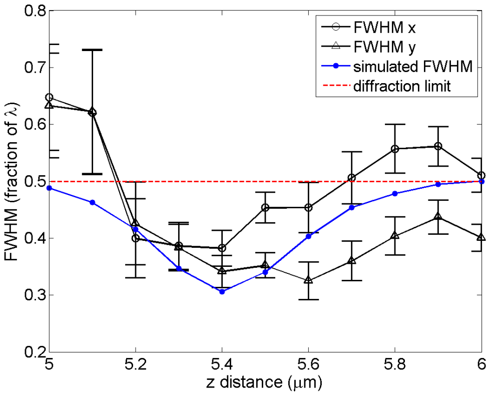

Figure 3.6: Comparison of the FWHM of the hotspot obtained from simulations (blue) and from measurements (black). Also the spotsize of the focal spot of a diffraction limited lens is shown (red).

The line profile in the experimental data was taken at an angle 45° as indicated in Fig. 3.1a, because the intensity of the peaks was a bit more symmetric along this direction than along x or y. For clarity, the line profile through the experimental data is shifted downwards to compensate for the background level. These line profiles do not overlap very well. In addition to the asymmetry in the experimental beam profiles, also the peak positions (corresponding to the sideband locations) do not overlap. It seems like the peaks in the simulations are closer together than in the experiments.

To verify this, we compare the x positions of the minima and maxima of the peaks in Fig. 3.7. The peak position as a function of the peak number (with the hotspot being peak number 0) is plotted in Fig. 3.8. The data are fitted with a linear function to determine the slopes and calculate the ratio of the slopes for experiments versus simulations. This gives a measure of

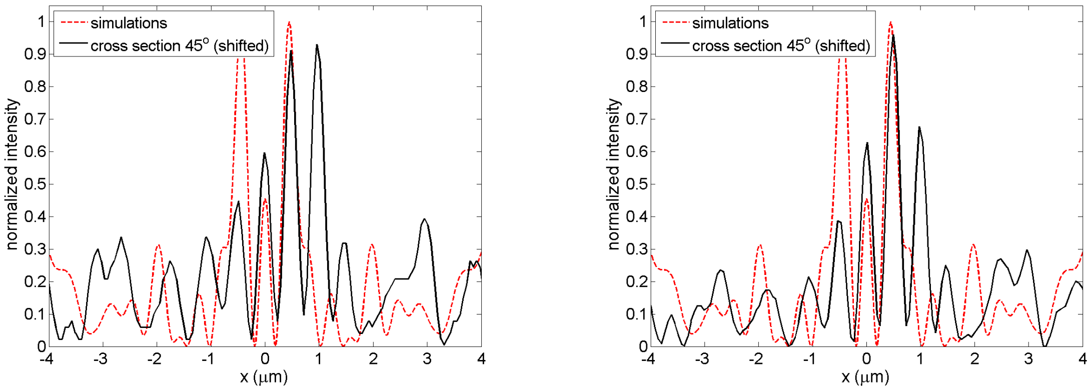

(a)

(b)

Figure 3.7: Lineprofiles through the center of the beamprofile in the focal plane at an angle of 45° (see Fig. 3.1a) for two different measurements. The central hotspot is defined to be at $x = 0$ so we can compare the sideband intensities and locations in the simulations (red) and measurements (black). The experimental data have an offset in intensity due to the background, and are therefore shifted downwards.

the factor with which the experiments differ from the simulations. The factor from the fits is approximately 1.5. Since we do not know the origin of the discrepancies, we can either multiply the x-axis of the simulated line profile by 1.5 or the x-axis of the experimental line profile by $1/1.5 = 0.67$. We have chosen the first option, and this results in the plot in Fig. 3.9. Here we see that the overlap between the experiments and simulations is better than before.

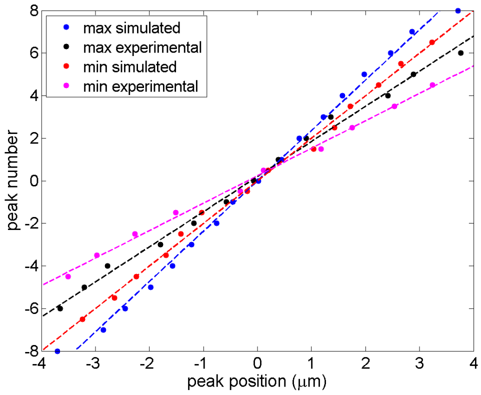

Figure 3.8: The peak numbers (the hotspot peak is defined as number 0) of the peaks in Fig. 3.7a as a function of the position. The positions of both the minima and the maxima of the peaks are plotted and a linear fit $ax + b$ is performed to estimate the slopes.

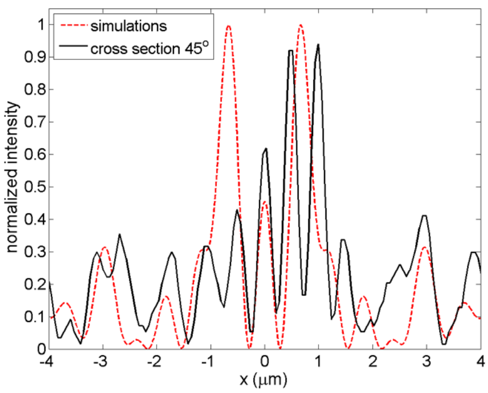

Figure 3.9: The same line profiles as in Fig. 3.7a but the x-axis of the simulated profile is multiplied by a factor 1.5 that was calculated from the slopes in Fig. 3.8.

3.1.3 Discussion

Our results show that the SOL is able to create a hotspot that is smaller than for a diffraction limited high NA lens. The hotspot size obtained by fitting the experimental data with a 2D Gaussian is in accordance with predictions from simulations, as we can see in Fig. 3.6.
However, as we can see in the intensity profiles in Fig. 3.2a and Fig. 3.2b, the intensity distribution is not symmetric. This becomes more clear when we look at Fig. 3.4, which shows the FWHM of the hotspot as a function of z distance. The FWHM in x and y are not always equal within the measurement error, as becomes clear from Fig. 3.6. This means that the hotspot in the images was asymmetric. However, the average FWHM in x and y seems to follow the theoretical curve quite well.
One explanation for the asymmetry is an improper alignment of the setup. Inspection of the sample while illuminating it via a 50:50 BS behind the objective lens (as explained in Sec. 2.1) yields the image shown in Fig. 3.10. This image shows that the SOL structure is nicely symmetric, as designed. If the SOL structure is rotationally symmetric, the interference pattern and thus the hotspot should be symmetric as well under normal incidence of the illumination beam. However, this image was made with an optical microscope, which means that the smallest features can not be resolved. Therefore, a second explanation for the asymmetry are manufacturing errors. If the structure is not perfectly symmetric, this will influence the symmetry of the interference pattern. To check how symmetric the SOL structure is, atomic force microscopy (AFM) measurements could be performed.

The same explanations can be used for the asymmetry observed in the positions of the sidebands in the line profiles of Fig. 3.7. In Fig. 3.11 the line profile of the interference pattern on the left and right of the hotspot are plotted on top of each other for comparison. For distances below 1 μm and beyond 7 μm from the hotspot center, the sidebands on the left ($x < 0$) and right ($x > 0$) of the hotspot are approximately symmetric. However, for $1 < |x| < 7$ μm this is not the case. To verify that misalignment is a cause of the observed asymmetries, measurements can be performed while tilting the sample in a controlled way.

The location in z where the hotspot size is minimal is usually called the focus of the SOL in literature, and we also used this term. However, the definition of a focus is the region to which all rays converge. For the SOL this is obviously not the case, so it can be argued whether “focus” is a good name. But if we consider the SOL to be a kind of lens, then the position where the hotspot is minimal is the best candiate to be the focus of the SOL.
The prediction from ASM simulations was that the focus is located at 5.4 μm from the SOL surface. Our method to estimate distances during the measurements involves focusing on the SOL surface with an objective lens. However, the depth of focus (DOF) of this lens is $DOF = \lambda/\mathrm{NA}^2 \approx 700$ nm, and that means that there is an inaccuracy in the distance estimation of ±350 nm. By carefully scanning in z to find a sharp image of the SOL surface as in Fig. 3.10 the inaccuracy in the distance estimation is reduced to approximately ±175 nm (half the DOF). This can explain why in our results the focus is located at 5.5 μm instead of the predicted 5.4 μm.

The quantitative comparison of the experiments with ASM simulations shows some discrepancies. We have seen that the positions of the sideband are a factor 1.5 larger in the experiments than for the simulations. By looking at the intensity behaviour of the hotspot in Fig. 3.2b

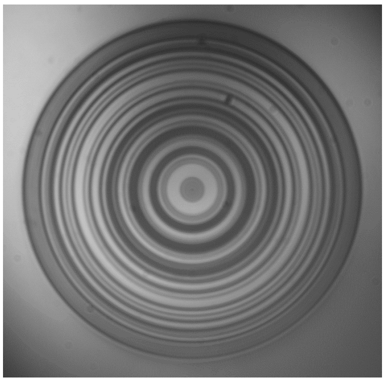

Figure 3.10: Image of the SOL mask made by illuminating with white light via the objective lens (as explained in Sec. 2.1), where we can see that the rings are circular and symmetric.

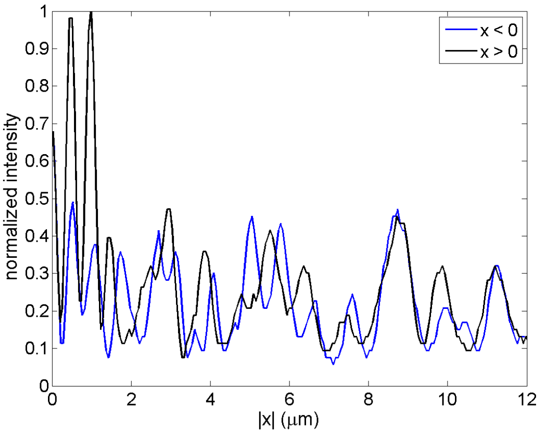

Figure 3.11: Plot of one of the line profiles from Fig. 3.7 where the line profile for $x > 0$ and $x < 0$ are plotted on top of each other to check the symmetry of the pattern.

and Fig. 3.5, we see a similar factor. In the beam profile from experiments, the locations where the hotspot has the highest intensity are approximately $6.5 - 4.5 = 2$ μm apart. In the simulated beamprofile this is approximately $6.2 - 4.8 = 1.4$ μm, which is approximately 1.5 times smaller than for the experiments.
We are not sure what the origin of these discrepancies is, and further experiments and analysis will be required to study this and to fully understand the SOL.

After a full characterization of the SOL, the next step is to use the SOL for super-resolution imaging. The plan was to illuminate test structures consisting of subwavelength slits or apertures with a collimated laser beam and pick up the signal with a SOL. These test structures have been designed, and a test setup and alignment strategy have been developed. However, due to a delay as the result of manufacturing, we have not yet been able to perform measurements. But in the near future we will start those measurements.

Chapter 4

Results from the optical metasurfaces

4.1 Lenses

Eight of the windows on the wafer contain an array of resonators designed to work as a lens: design #1 to #8. They impose a parabolic phase profile as in Eq. 1.8 onto the incident light, and focus the light to a spot at 2 μm from the surface. As described in Sec. 2.2, half of the arrays consists of 120x120 Si resonators (large arrays), while the rest consists of 17x17 resonators (small arrays). The results of the characterization of the beam profile of light transmitted by these lenses are presented in this chapter.

4.1.1 Large arrays

The arrays with 120x120 resonators cover an area of 45x45 μm^2. With the setup as described in Sec. 2.2 we have performed measurements on the light transmitted by the samples. Two examples of the recorded beam profile for sample #3 at different distances from the surface are shown in Fig. 4.1.

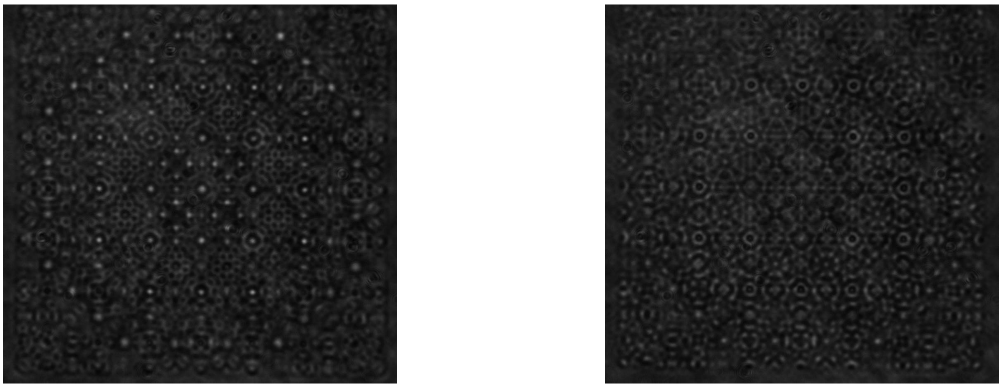

(a) (b)

Figure 4.1: The interference pattern of light transmissted by sample #3 at different distances from the surface. In addition to the central spot, a pattern of many spots is observed over an area similar to the area of the sample.

These images show that the interference pattern produced by the resonators is not a single focus as expected, but a pattern covering the full area of 45x45 μm^2. Fig. 4.2 shows a scanning electron microscopy (SEM) picture of design #1 (which is equal to #2 to #4 except for the height of the Si resonators) in comparison with the transmission spectrum from Fig. 4.1b. The observed interference pattern shows many similarities with the geometrical structure of the array of resonators, as indicated in Fig. 4.2.

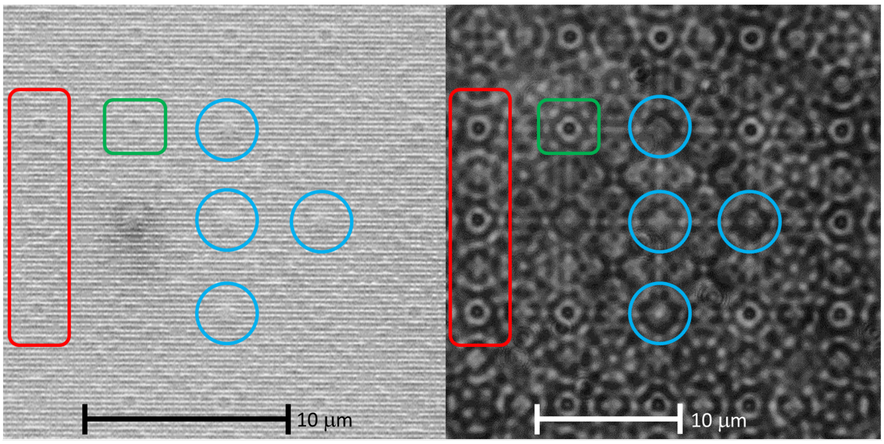

Figure 4.2: Comparison of a scanning electron microscopy (SEM) picture of the array of resonators from design #1 (left), made by the Else Kooi lab, and the pattern of transmitted light from design #3 (right). The diameter of the resonators is varying throughout the array in order to impose the required phase profile, which gives rise to the pattern we observe in the SEM image. Some of the features appearing in both images are indicated to guide the eye.

The next step was to make a scan in z (along the optical axis) and record the corresponding beam profiles to create an xz and yz intensity profile. Due to the symmetry of the interference pattern, these images are similar. As an example, the xz intensity profile is shown in Fig. 4.3. Note that the z distance is a relative distance in this figure, which means that the optical metasurface is not at $z = 0$ but at an arbitrary location.
In this figure, we see that the spots we also observe in Fig. 4.1 change in spot diameter and intensity. Zooming in on the behavior of the central spot of the pattern results in Fig. 4.4.

The behavior of this central spot reminds of that of a focal spot, therefore the FWHM and the intensity (both obtained by fitting a 2D Gaussian, Eq. 2.1, to the spot) are plotted as a function of z, as shown in Fig. 4.5 and Fig. 4.6. These figures show that at a certain distance from the lens surface, the intensity is maximum while the spotsize is minimum.
This focusing behavior was not only observed for the central spot, but also for some of the additional spots. Although they do not have their minimum spotsize at the same distance from the lens as the central spot.

Characteristics of a conventional lens are that the intensity is maximum in the focus, while the spotsize is minimum, which is what we observe for the central spot of the pattern created by the optical metasurface. For a better comparison of the focusing behavior we take a line profile in the focal plane through the central spot, which is shown in Fig. 4.7. From this plot we can estimate that the signal-to-noise ratio (SNR) for this focus is approximately $\frac{1}{0.5} = 2$. For further characterization of the focus, an Airy pattern (Eq. 2.3 in Sec. 2.2) is fitted to the central spot in Fig. 4.7 as is shown in Fig. 4.8. From this fit a measure of the effective NA can be obtained, which is $\mathrm{NA}_x = 0.56 \pm 0.01$ and $\mathrm{NA}_y = 0.51 \pm 0.01$.

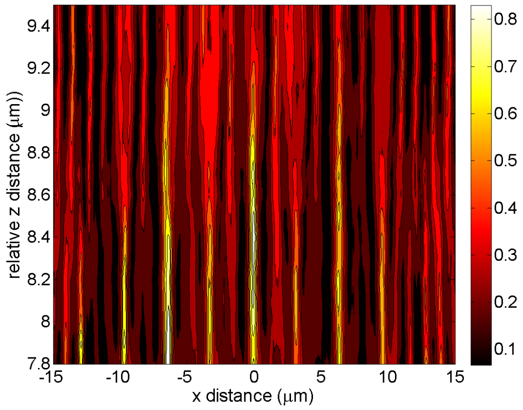

Figure 4.3: The xz intensity profile created by design #4. The intensity and width of the central spot (at $x = 0\mu$m) and other spots from the interference pattern are changing with z. Note that the z distance is a relative distance, which means that the surface of the optical metasurface is not at $z = 0$ but at an arbitrary position.

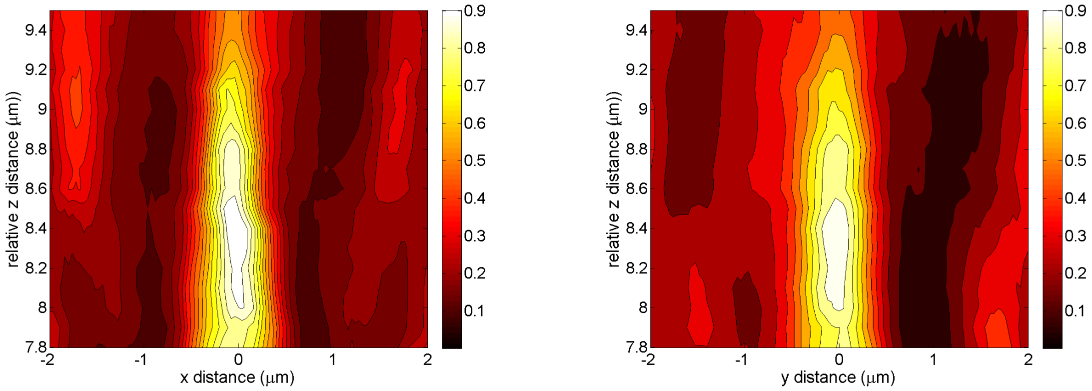

(a) **(b)**

Figure 4.4: Zoom on the central spot in the intensity profile from Fig. 4.3. Both the xz (a) and yz (b) intensity profiles are shown. These are quite similar, and in both images the central spot behaves like a focal spot. Note that, as in Fig. 4.3, the z distance is a relative distance.

Explanation with simulations

Since the arrays are not working as a lens as expected, ASM simulations have been used to explain the appearance of multiple spots. Those simulations show that the extra spots are not the result of diffraction orders. Instead, the problem is related to the steep phase profile of the lens.

The phase only has a meaning if it is modulo 2π. In one dimension, the phase profile is $\phi = \frac{k_o}{2f}x^2$, which is quite steep for larger values of x (see Fig. 4.9). When we plot the phase profile modulo 2π, we obtain the graph in Fig. 4.9. Fig. 4.10 shows that by sampling with 377 nm (the periodicity of our lattices), the 2π phase jumps of the parabola far from the center of the parabola are not covered. The sampled points of the parabola do not follow the desired phase profile, but instead different parabolas are formed. This suggests that the

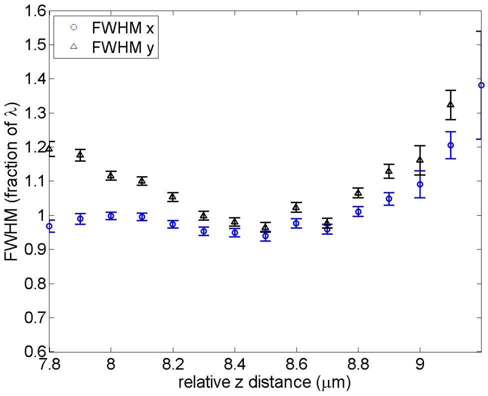

Figure 4.5: The FWHM gives an indication of the diameter of the spot. It is obtained by fitting a 2D Gaussian to the central spot in images like Fig. 4.1 taken at different distances from the lens surface.

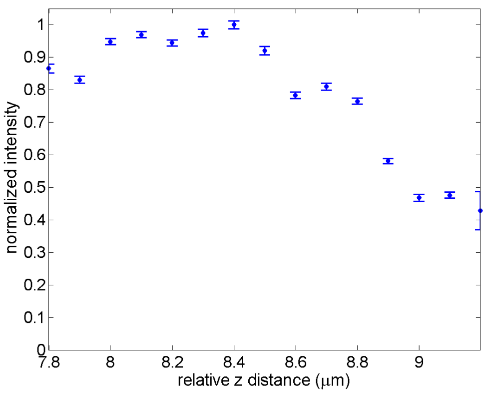

Figure 4.6: The intensity is obtained by fitting a 2D Gaussian to the central spot in images like Fig. 4.1 taken at different distances from the lens surface.

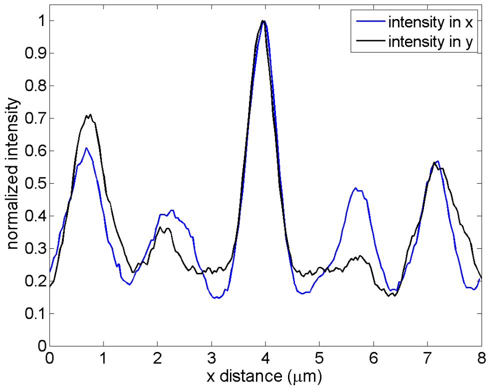

Figure 4.7: Line profile in the focal plane through the central spot of the pattern created by the optical metasurface.

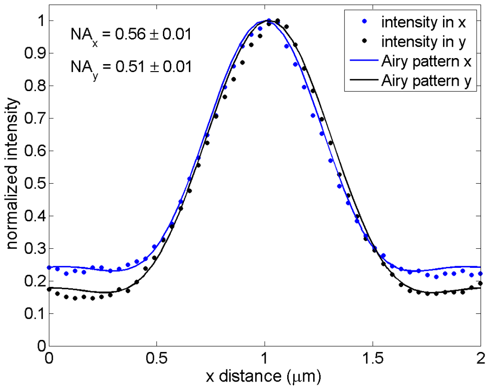

Figure 4.8: Fit of an Airy pattern (Eq. 2.3 to the central peak in Fig. 4.7 to determine the effective NA.

extra spots in Fig. 4.1 are the result of aliasing. The fact that there are parts of the phase profile that are parabolic, explains why we still observed focusing behavior of the lens.
To prevent the aliasing effects, each 2π phase jump should be sampled by at least two points. This is taken into account in the design of the new optical metasurfaces that will be tested soon.

4.1.2 Small arrays

Although the performance of the optical metasurfaces consisting of 120x120 resonators is limited by aliasing, we can still take a look at the smaller arrays. The arrays with 17x17 resonators cover an area of 6.4x6.4μm^2, which is almost 50 times smaller than for the large arrays. Therefore the resonators only sample the less steep part of the parabola, for which the 377 nm sampling is sufficient (see Fig. 4.10), and only one focus is formed.

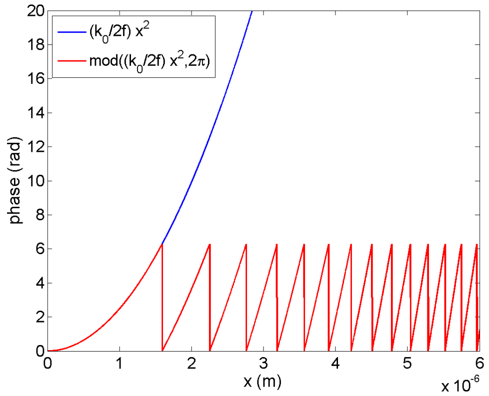

Figure 4.9: The desired parabolic phase profile of the optical metasurface lenses (blue) and the same phase profile modulo 2π (red).

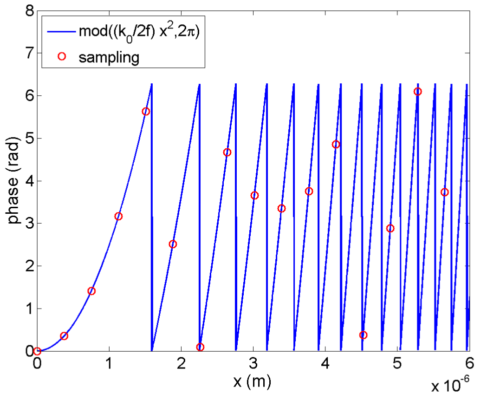

Figure 4.10: The parabolic phase profile modulo 2π from Fig. 4.9 in blue with the red datapoints indicating the sampling by the Si resonators in the array with a periodicity of 377 nm.

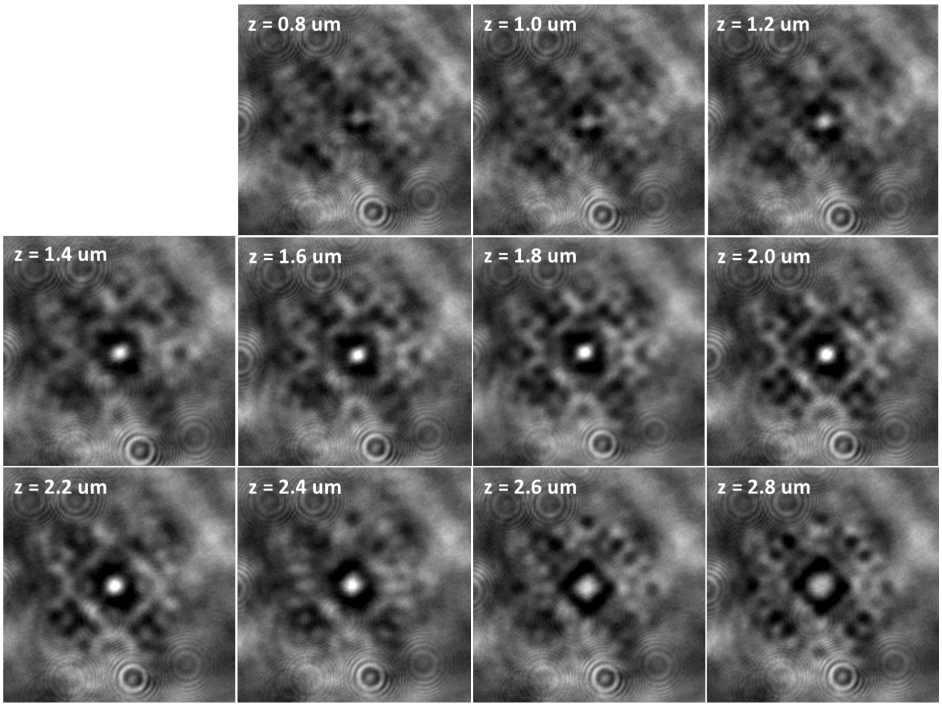

Figure 4.11: Beam profiles of light transmitted by sample #7 imaged at different distances from the sample surface. The size and intensity of the spot are varying, and according to the design a focal spot should be created at 2 μm from the lens.

With the setup as described in Sec. 2.2 we have performed measurements on the light transmitted by the samples. During the measurements, the waveplate was not in the setup, and only the PBS in the illumination optics was used to control the polarization of the incident light. Some examples of the recorded beam profile for sample #7 at different z distances from the surface are shown in Fig. 4.11. It becomes clear that the intensity and size of the central spot are varying with distance z. This can be studied in more detail by fitting a 2D

Gaussian to the central spot to obtain a FWHM and a peak intensity. The graphs with the FWHM and intensity as a function of z are shown in Fig. 4.12 and Fig. 4.13 respectively. These figures show that the minimum FWHM is reached at approximately 1.7 μm from the surface and that the maximum intensity is reached at approximately the same distance. This indicates that the optical metasurface is focusing the light similar to a conventional lens. In addition, a parabola ($ax^2 + b$) is fitted to a small range around the focus ($1 < z < 2.5$ μm). The fit shows that the FWHM has a parabolic dependence on z in this range, as one would expect for a conventional lens (as explained in Sec. 2.2.

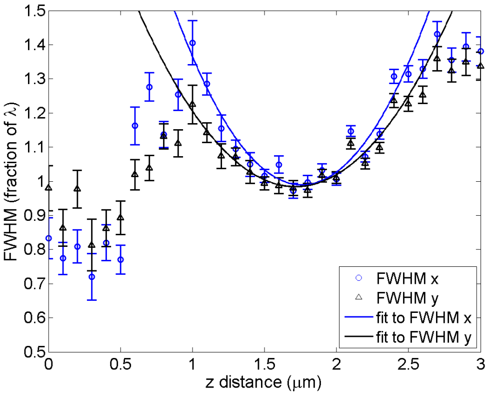

Figure 4.12: The relation between the FWHM of the spot and the z distance from the lens surface. The intensity was obtained by fitting a 2D Gaussian to the spots in the beamprofiles from Fig. 4.11. A parabola $ax^2 + b$ is fitted to the data in the range $1 < z < 2.5$ μm.

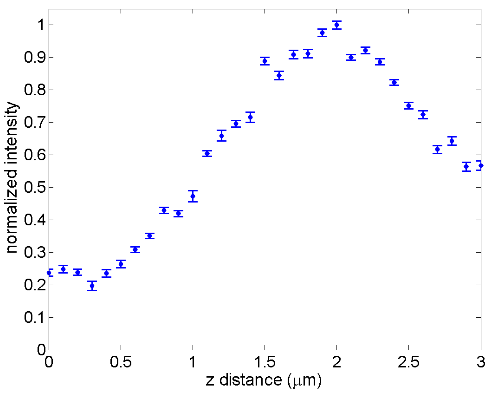

Figure 4.13: The relation between the intensity of the spot and the z distance from the lens surface. The intensity was obtained by fitting a 2D Gaussian to the spots in the beamprofiles from Fig. 4.11.

To compare the performance with that of a conventional lens, we can take a look at the line profile through the center of the spot, as shown for design #7 in Fig. 4.14. This line profile provides a measure for the signal-to-noise ratio (SNR) of the lens. The SNR is calculated by dividing the peak intensity from the spot by the intensity of the noise peaks. For this sample, the SNR is approximately 2.0. Compared to the SNR of approximately 60 for an Airy pattern, this is very low.

Next, an Airy pattern (Eq. 2.3) is fitted to the central peak, as shown in Fig. 4.15 to provide an estimated value of the effective NA of the metasurface lens. For this sample, we find $\mathrm{NA}_{eff} = 0.56 \pm 0.02$.

Similar measurements and data analysis are performed on sample #5 to #8, which are equal in design except for the height of the resonators (as explained in Sec. 2.2). The results of the four samples are displayed in table 4.1. All designs perform equally good in terms of the FWHM of the spot in focus. Also the effective NA is similar, but for design #5 it is lower. Finally, the values for the SNR are close, but here design #7 has a lower SNR.

In theory, the lenses should not influence the polarization of the light, and the polarization of the incident light should also not influence the performance of the metasurface lenses.

To check the first fact, a second PBS was placed in the setup (see Fig. 2.8) and rotated

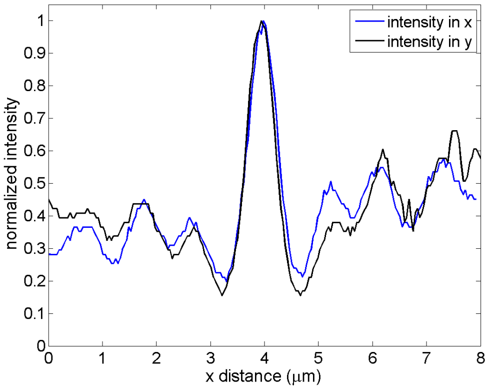

Figure 4.14: Line profile through the focus of the beam profile of light transmitted by design #7 in x (blue) and y (black). The ratio between the intensities of the central spot and the additional features provide a measure of the SNR of the sample.

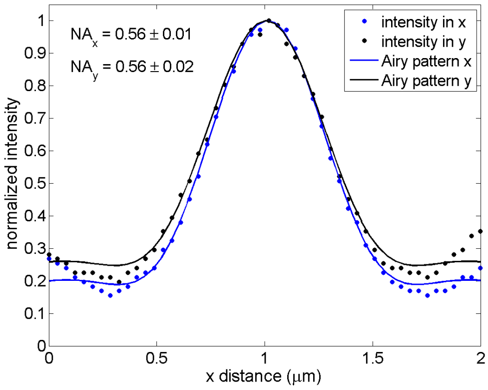

Figure 4.15: Zoom on the data from the central peak from Fig. 4.14 (dots) with a fit of the Airy pattern (solid lines).

	Design #5	Design #6	Design #7	Design #8
FWHM$_x$	1.05 ± 0.01 λ	0.91 ± 0.01 λ	0.97 ± 0.02 λ	0.98 ± 0.01 λ
FWHM$_y$	1.03 ± 0.01 λ	1.03 ± 0.02 λ	0.98 ± 0.02 λ	0.86 ± 0.01 λ
NA$_{eff}$	0.48 ± 0.02	0.53 ± 0.02	0.56 ± 0.02	0.54 ± 0.01
SNR	2.9	2.5	2.0	2.5

Table 4.1: Summary of the results from experiments on four different samples (design #5 to #8) that should work as a lens, each located on a different quadrant of the wafer.

over 360°. The result is pictured in Fig. 4.16 and Fig. 4.17. These figures show that the polarization of the transmitted light is as expected under rotation of the 2$^{\text{nd}}$ PBS ($cos^2(\theta)$ behavior) and that no clear relation is found between the FWHM and the angle of the PBS. To check the second fact, the second PBS is removed and a half-wave plate (HWP) is placed in the illumination optics (see Fig. 2.8). The HWP is rotated over 180° to change the polarization of the incident light. The results in Fig. 4.18 and Fig. 4.19 show that both the intensity and FWHM of the central spot do not show a clear dependence of the angle θ_{HWP}.

4.2 Polarizing metasurfaces

Design #9 to #14 are metasurfaces consisting of elliptical resonators at an angle of 45° with the polarization of the incident light. They are designed to change the linearly polarized incident light into circularly polarized light, so they are the equivalent of a quarter-wave plate. Design #15 and #16 are the polarization scramblers. Because of the randomly oriented elliptical resonators, they are expected to convert polarized light into (partly) depolarized light.

The polarization of light transmitted by an optical metasurface can be studied with a PBS

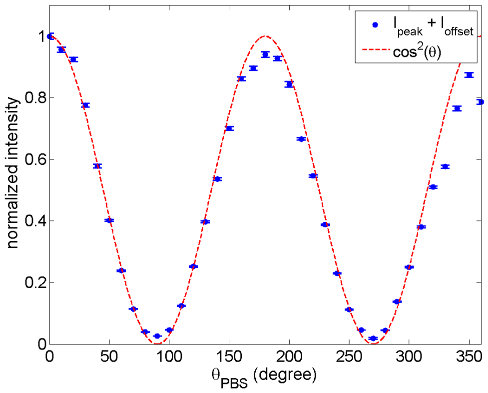

Figure 4.16: Intensity of the spot in the beam-profile of light transmitted by design #8 as a function of the angle of the second PBS θ_{PBS} (blue dots). The theoretical relation for the intensity as a function of θ_{PBS} is $cos^2(\theta_{PBS}$ and is shown with the red dotted line.

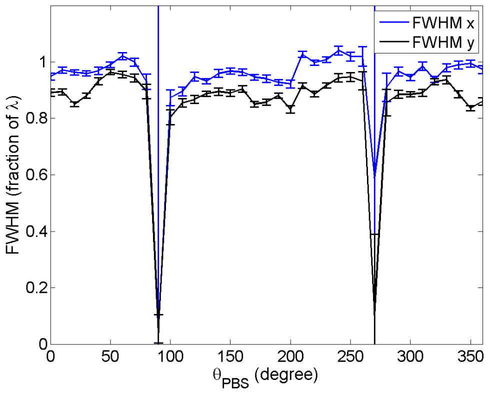

Figure 4.17: FWHM of the spot in the beam-profile of light transmitted by design #8 as a function of the angle of the second PBS θ_{PBS}.

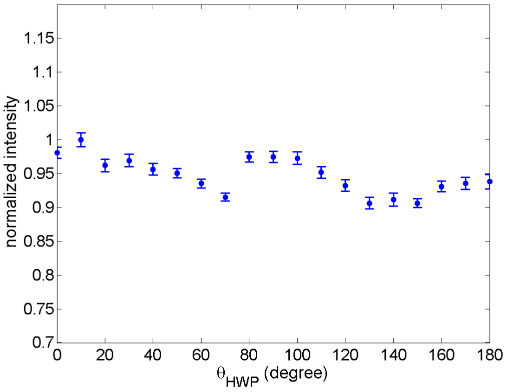

Figure 4.18: Intensity of the spot in the beam-profile of light transmitted by design #8 as a function of the angle of the HWP θ_{HWP}.

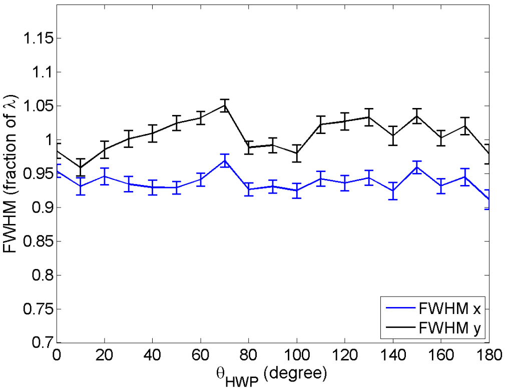

Figure 4.19: FWHM of the spot in the beam-profile of light transmitted by design #8 as a function of the angle of the HWP θ_{HWP}.

in the illumination path and a second PBS in the detection path (see Fig. 2.8). The second PBS can be rotated to an angle of 90° with respect to the first one. If the metasurface has no influence on the polarization, then no light will be detected. However, if the metasurface converts linearly polarized light into circularly polarized light or unpolarized light, part of the light will be transmitted through the second PBS.

Measurements have been performed on all six samples, but their performance was not as predicted. Fig. 4.20 shows the transmitted light through sample #15 as a function of the angle of the second PBS (θ_{PBS}). During the measurements, a quarter waveplate (QWP) was in the illumination path at 45° with respect to the polarization of the incident light. The measurements are repeated without the sample, and we can see that the results are equal. This means that the metasurface did not influence the polarization of the light. Results for the other metasurfaces show a similar trend.

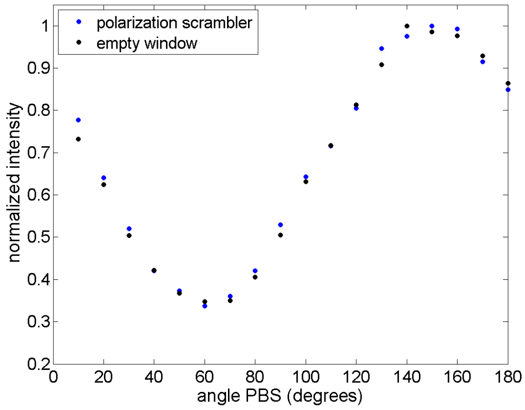

Figure 4.20: The intensity of light transmitted by the full area of the metasurface polarization scrambler #15 as a function of the angle of the second PBS θ_{PBS}. Results are plotted for the array of resonators of design #15 (blue) and for an empty window of the wafer (black) that should not influence the polarization.

Important to mention is that the behavior in this plot is not as expected with a QWP at 45° in between two PBSs. We would expect a flat intensity profile when θ_{PBS} is varied. Additional experiments on the QWP showed that this was not working very well and converted linearly polarized light into light with elliptical polarization instead of circular. But since the graphs in Fig. 4.20 with and without sample overlap, the conclusion does not change.

4.3 Discussion

Our results show that the optical metasurface lenses consisting of 120x120 resonators create multiple foci instead of only one as predicted. The explanation for this effect is undersampling of the phase profile. In the design for the next wafer, this is taken into account by increasing the focal distance so the phase profile in Eq. 1.8 will be less steep and the sampling of 377 nm is enough to follow the phase profile.

Apart from this, the metasurface lenses did produce a nice focus with a parabolic FWHM(z) relation (see Fig. 4.12) and the highest intensity of the hotspot corresponds to the smallest spotsize. These results show that the optical metasurface lenses have a performance similar to conventional lenses. In addition, table 4.1 shows that the designs located on the four different quadrants of the wafer (with a different resonator height) show similar performances. This means that the design of these metasurface lenses are quite robust to manufacturing tolerances.

Fitting an Airy pattern to the line profile of the focus (Fig. 4.15) indicated that the effective NA of lens #7 is approximately 0.56 ± 0.02. This value is smaller than the expected NA of 0.86 that was calculated for a diffraction limited lens with the same dimensions (see Sec. 1.2.3) [28]. This means that our metasurface lenses are not diffraction limited, which is not surprising since also other factors (like imperfections in the manufacturing) will limit the resolution.

The focus of the lenses was measured to be at approximately 1.7 μm from the lens surface, while it was expected at $f = 3\lambda = 1.9$ μm according to the design (see Sec. 1.2.3) [28]. As for the SOL measurements, there is also an experimental inaccuracy of ±150 nm for the distance estimations (see Sec. 3.1.3), which can explain this difference. Moreover, HFSS simulations of a finite array of 17x17 resonators (Sec. 1.2.3) showed that the focus lies closer to the lens than designed [28].

In Fig. 4.11 we can see that the focal spot is surrounded by a darker region. Around this region, interference features are visible. These are quite intense and reduce the SNR, as we can see in Fig. 4.14. The features can be attributed to two effects. First, the diameter of the illumination beam was 0.87 mm, while the resonator area was only 6.4x6.4 μm^2. Therefore we have a high background signal. To prevent this, the design was to cover the sample with a thin layer of titanium leaving a 6.4x6.4 μm^2 window at the position of the resonators. Due to manufacturing problems, this is not the case. In a next wafer, the titanium film should be applied. Second, the array consists of only 17x17 resonators. This means that the boundary effects of the edges of the array will play a role. These interference effects appear at a certain distance from the hotspot, leaving a dark zone of approximately 500 nm around the hotspot.

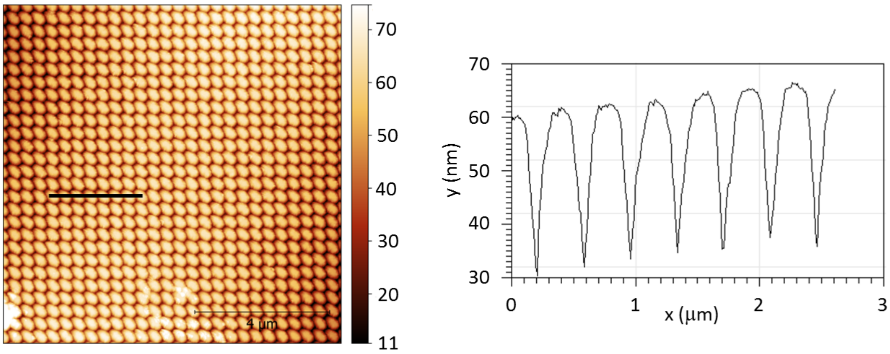

Figure 4.21: Image created with sub-surface AFM of one of the metasurface quarter waveplates (left) and a line profile along the black line (right). The resonators are at an angle of 45° and the scale on the right indicates that the height of the resonators is less than the designed 96 nm.

The metasurface lenses are performing quite well, but this is not the case for the waveplates and polarization scramblers. These did not show any influence on the polarization. To find out why, some sub-surface AFM measurements have been performed. Fig. 4.21 shows the result for one of the waveplate samples. The resonators are all oriented at an angle of 45°, as designed, but a line profile of this image shows that the height of the resonators is approximately 60 nm instead of 96 nm. However, since the resonators are embedded in SiO_2, it is difficult to accurately measure their height. Nevertheless, HFSS simulations on elliptical resonators with $h_c = 60$ nm show that the component of the polarization orthogonal to the incident polarization is significantly reduced. Since the background signal is relatively high in our measurement, such a low signal will not be detected. If this is the case, this provides an explanation why we did not detect any influence of the metasurface waveplates and polarization scramblers on the polarization.

In the next wafer, the height of the resonators will be measured with AFM before the top layer of SiO_2 is applied. Further measurements are required to verify the performance of the metasurface waveplates and polarization scramblers. In future experiments, we will also study

the wavelength dependence of the performance of the optical metasurfaces by illuminating with different wavelengths.
Important to note is that if the height of the resonators is not as designed, than this is also the case for the resonators of the metasurface lenses (design #1 to #8), and that probably influences the performance of these lenses as well.

Chapter 5

Conclusions

In this project, we studied two types of non-conventional optical devices. The super-oscillatory lens (SOL) and several optical metasurfaces.

The super-oscillatory lens

The SOL is an amplitude mask consisting of binary concentric rings in a 100 nm titanium film. Light transmitted by the SOL creates an interference pattern with a central hotspot and multiple sidebands. The promising property of a SOL is that this hotspot can be smaller than the focus of a diffraction limited lens ($\lambda/2$). Our measurements have shown that the SOL creates a hotspot with a spotsize as small as $(0.34 \pm 0.03)\lambda$. Moreover, the hotspot size is smaller than $\lambda/2$ over a range of almost 1 μm. The results confirm that the smallest hotspot comes with the lowest intensity, which is in accordance with SOL theory.
Comparison of our results with simulations showed that qualitatively they behave similar. However, quantitatively, there are some discrepancies in the x, y and z distances. For all three directions, the distances in the simulated intensity profiles are 1.5 times smaller than in the measured profiles. To fully understand the SOL, further experimental and theoretical analysis of these differences will be necessary.

The final goal is to use the SOL for confocal super-resolution imaging, so the next step in our experiments is imaging with the SOL. Because of the intense sidebands and the low intensity of the hotspot, post processing and calibration will be required. We are currently working on a setup to image sub-wavelength test structures (slits and apertures in a metal film). Two scenarios will be tested: illumination of the test structures with the SOL and detection with a conventional objective lens (like Rogers et al. [7]), and illumination with plane waves and detection with the SOL.

Optical metasurfaces

The optical metasurfaces consist of arrays of cylindrical Si resonators embedded in a SiO_2 substrate. The biggest advantage of these metasurfaces is that they are extremely thin (665 nm), but nevertheless can be designed to have similar performance as conventional optics. The light transmitted by the metasurfaces has been characterized.
We have shown that metasurface lenses consisting of 17x17 resonators have a performance

similar to conventional lenses, with a FWHM of approximately 1λ, a SNR around 2.5 and an effective NA of approximately 0.54. This NA is lower than for a diffraction limited lens with the same dimensions and focal distance, so our lenses are not diffraction limited. Except from this, the metasurfaces perform as expected from the design. The designs located on the four different quadrants of the wafer (with a different resonator height) show similar performances. This means that the design of these metasurface lenses are quite robust to manufacturing tolerances.

The lenses consisting of 120x120 resonators create a pattern with multiple spots instead of a single focus. Analysis has shown that this is most likely the result of undersampling the parabolic phase profile, and measurements on a new sample with less steep phase profile will be performed to prove this hypothesis. Besides the additional spots, experiments have shown that the central spot and several of the extra spots do behave like a focus.

The metasurface quarter waveplates and polarization scramblers also did not perform as expected. Our results showed that they did not influence the polarization of the incident light. This was most likely because the height of the resonators might have been 40% lower than designed, causing the transmission of cross polar components to be too low to detect. Characterization of the height of the resonators and the transmission of the samples in the new wafer are required to confirm this hypothesis. But since the metasurface lenses perform quite well, we expect that the structures with a different purpose (like the quarter waveplates) will also work in the future.

Bibliography

[1] Eugene Hecht. *Optics*. Addison Wesley, 4 edition, 2002.

[2] John Brian Pendry. Negative refraction makes a perfect lens. *Physical Review Letters*, 85(18):3966, 2000.

[3] Lukas Novotny and Bert Hecht. *Principles of Nano-Optics*. Cambridge University Press, 1 edition, 2006.

[4] David R Smith, John B Pendry, and Mike CK Wiltshire. Metamaterials and negative refractive index. *Science*, 305(5685):788–792, 2004.

[5] MV Berry and S Popescu. Evolution of quantum superoscillations and optical super-resolution without evanescent waves. *Journal of Physics A: Mathematical and General*, 39(22):6965, 2006.

[6] Nikolay I Zheludev. What diffraction limit? *Nature Materials*, 7(6):420–422, 2008.

[7] Edward TF Rogers, Jari Lindberg, Tapashree Roy, Salvatore Savo, John E Chad, Mark R Dennis, and Nikolay I Zheludev. A super-oscillatory lens optical microscope for subwavelength imaging. *Nature Materials*, 11(5):432–435, 2012.

[8] Paulo JSG Ferreira and Achim Kempf. Superoscillations: faster than the nyquist rate. *Signal Processing, IEEE Transactions on*, 54(10):3732–3740, 2006.

[9] Fu Min Huang, Yifang Chen, F Javier Garcia de Abajo, and Nikolay I Zheludev. Optical super-resolution through super-oscillations. *Journal of Optics A: Pure and Applied Optics*, 9(9):S285, 2007.

[10] Edward TF Rogers, Salvatore Savo, Jari Lindberg, Tapashree Roy, Mark R Dennis, and Nikolay I Zheludev. Super-oscillatory optical needle. *Applied Physics Letters*, 102(3):031108, 2013.

[11] Edward TF Rogers and Nikolay I Zheludev. Optical super-oscillations: sub-wavelength light focusing and super-resolution imaging. *Journal of Optics*, 15(9):094008, 2013.

[12] Tapashree Roy, Edward TF Rogers, Guanghui Yuan, and Nikolay I Zheludev. Point spread function of the optical needle super-oscillatory lens. *Applied Physics Letters*, 104(23):231109, 2014.

[13] Guanghui Yuan, Edward TF Rogers, Tapashree Roy, Giorgio Adamo, Zexiang Shen, and Nikolay I Zheludev. Planar super-oscillatory lens for sub-diffraction optical needles at violet wavelengths. *Scientific Reports*, 4(6333):10.1038, 2014.

[14] Nanbo Jin and Yahya Rahmat-Samii. Advances in particle swarm optimization for antenna designs: Real-number, binary, single-objective and multiobjective implementations. *Antennas and Propagation, IEEE Transactions on*, 55(3):556–567, 2007.

[15] Joseph W. Goodman. *Introduction to Fourier Optics*. The McGraw-Hill Companies, inc., 2 edition, 1996.

[16] Nanfang Yu and Federico Capasso. Flat optics with designer metasurfaces. *Nature Materials*, 13(2):139–150, 2014.

[17] Nanfang Yu, Patrice Genevet, Mikhail A Kats, Francesco Aieta, Jean-Philippe Tetienne, Federico Capasso, and Zeno Gaburro. Light propagation with phase discontinuities: generalized laws of reflection and refraction. *Science*, 334(6054):333–337, 2011.

[18] Nanfang Yu, Patrice Genevet, Francesco Aieta, Mikhail Kats, Romain Blanchard, Guillaume Aoust, J-P Tetienne, Zeno Gaburro, Federico Capasso, et al. Flat optics: Controlling wavefronts with optical antenna metasurfaces. *Selected Topics in Quantum Electronics, IEEE Journal of*, 19(3):4700423–4700423, 2013.

[19] Xingjie Ni, Satoshi Ishii, Alexander V Kildishev, and Vladimir M Shalaev. Ultra-thin, planar, babinet-inverted plasmonic metalenses. *Light: Science & Applications*, 2(4):e72, 2013.

[20] Isabelle Staude, Andrey E Miroshnichenko, Manuel Decker, Nche T Fofang, Sheng Liu, Edward Gonzales, Jason Dominguez, Ting Shan Luk, Dragomir N Neshev, Igal Brener, et al. Tailoring directional scattering through magnetic and electric resonances in subwavelength silicon nanodisks. *ACS Nano*, 7(9):7824–7832, 2013.

[21] Andrey B Evlyukhin, Sergey M Novikov, Urs Zywietz, Rene Lynge Eriksen, Carsten Reinhardt, Sergey I Bozhevolnyi, and Boris N Chichkov. Demonstration of magnetic dipole resonances of dielectric nanospheres in the visible region. *Nano Letters*, 12(7):3749–3755, 2012.

[22] F. Silvestri, E. Pisano, G. Gerini, V. Lancelotti, and V. Galdi. Nanoresonator based dielectric surfaces for light manipulation. In *The 45th European Microwave Conference*, September 2015.

[23] J Van de Groep and A Polman. Designing dielectric resonators on substrates: Combining magnetic and electric resonances. *Optics Express*, 21(22):26285–26302, 2013.

[24] Sonny Vo, David Fattal, Wayne V Sorin, Zhen Peng, Tho Tran, and RG Beausoleil. Subwavelength grating lenses with a twist. *IEEE Photonics Technology Letters*, 26(13):1375–1378, 2014.

[25] Paul R West, James L Stewart, Alexander V Kildishev, Vladimir M Shalaev, Vladimir V Shkunov, Friedrich Strohkendl, Yuri A Zakharenkov, Robert K Dodds, and Robert Byren. All-dielectric subwavelength metasurface focusing lens. *Optics Express*, 22(21):26212–26221, 2014.

[26] Amir Arbabi, Yu Horie, Alexander J Ball, Mahmood Bagheri, and Andrei Faraon. Subwavelength-thick lenses with high numerical apertures and large efficiency based on high-contrast transmitarrays. *Nature Communications*, 6(7069):1–7, 2015.

[27] Francesco Aieta, Mikhail A Kats, Patrice Genevet, and Federico Capasso. Multiwavelength achromatic metasurfaces by dispersive phase compensation. *Science*, 347(6228):1342–1345, 2015.

[28] F. Silvestri, G. Gerini, E. Pisano, and V. Galdi. High numerical aperture all-dielectric metasurface micro-lenses. In *Antennas and Propagation USNC/URSI National Radio Science Meeting, 2015 IEEE International Symposium on*, pages 1030–1031, July 2015.

Chapter 6

Appendix

6.1 Dimensions of the SOL structure

The SOL consists of 25 concentric rings with binary amplitude, as was explained in Sec. 1.1.1 and Sec. 2.1. The exact dimensions of the rings that are etched from the titanium film are summarized in Tab. 6.1.

6.2 Production of the optical metasurfaces

The optical metasurfaces have been manufactured in five steps, as is visualized in Fig. 6.1. An overview of the design details for all 16 different designs is summarized in Tab. 6.2.

	Inner radius (nm)	Outer radius (nm)
1	0	200
2	400	600
3	800	1000
4	1200	1400
5	3000	3200
6	3400	3600
7	4000	5000
8	5800	6000
9	6200	7400
10	7800	8000
11	8600	9000
12	9200	10000
13	10400	10800
14	11600	12000
15	12400	12600
16	13600	14000
17	14400	14600
18	15000	15400
19	16000	16600
20	16800	17000
21	17400	17800
22	18000	18200
23	18400	18600
24	18800	19000
25	19200	19600

Table 6.1: The inner and outer radii of the concentric rings that are etched from the titanium film to create the SOL.

Design	Function	N	h_c (nm)	Shape	θ_{res}	Radius (nm)	A (nm)	B (nm)
1	lens	120x120	102	circle	-	35 - 135	-	-
2	lens	120x120	100	circle	-	35 - 135	-	-
3	lens	120x120	96	circle	-	35 - 135	-	-
4	lens	120x120	93	circle	-	35 - 135	-	-
5	lens	17x17	102	circle	-	35 - 135	-	-
6	lens	17x17	100	circle	-	35 - 135	-	-
7	lens	17x17	96	circle	-	35 - 135	-	-
8	lens	17x17	93	circle	-	35 - 135	-	-
9	$\lambda/4$-plate	120x120	102	ellipse	45°	-	338	104.8
10	$\lambda/4$-plate	120x120	100	ellipse	45°	-	338	98
11	$\lambda/4$-plate	120x120	96	ellipse	45°	-	232	132.2
12	$\lambda/4$-plate	120x120	93	ellipse	45°	-	216	149
13	$\lambda/4$-plate	120x120	100	ellipse	45°	-	210	163.8
14	$\lambda/4$-plate	120x120	96	ellipse	45°	-	204	140.8
15	scrambler	120x120	100	ellipse	var.	-	338	98
16	scrambler	120x120	96	ellipse	var.	-	232	132.2

Table 6.2: Overview of the characteristics of the 16 different designs on the wafer: the function (lens, quarter waveplate or polarization scrambler), number of resonators (N), height of the resonators (h_c), shape (circular or elliptical), orientation (θ_{res} can be 45° or variable), radius and the long (A) and short (B) axes of the resonators.

(a) The process starts with an SOI wafer.

(b) Reactive ion etching to create the pattern of Si resonators.

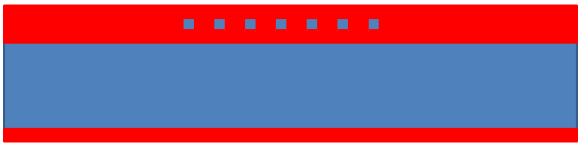

(c) Deposition of SiO_2 via plasma enhanced chamical vapor deposition.

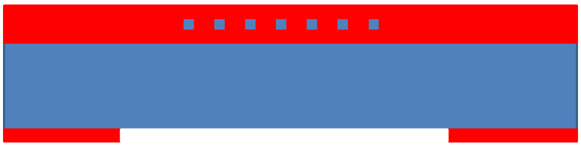

(d) Patterning of the backside of the wafer.

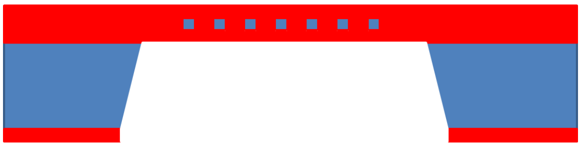

(e) Deep reactive ion etching of the SiO_2.

Figure 6.1: Schematic representation of the five production steps to manufacture an optical metasurface from an SOI wafer. In these pictures, red is Si and blue is SIO_2.